Geophysical Journal International

Geophys. J. Int. (2016) **206,** 438–456
Advance Access publication 2016 April 26
GJI Mineral physics, rheology, heat flow and volcanology

doi: 10.1093/gji/ggw154

Brittle and semi-brittle behaviours of a carbonate rock: influence of water and temperature

A. Nicolas,[1] J. Fortin,[1] J.B. Regnet,[1] A. Dimanov[2] and Y. Guéguen[1]

[1]*Laboratoire de Géologie, Ecole Normale Supérieure - PSL Research University, CNRS, UMR* 8538, *Paris, France. E-mail: aurelien.nicolas89@gmail.com*
[2]*Laboratoire de Mécanique des Solides, UMR* 7649, *Ecole Polytechnique, Bat* 65, *Route de Saclay, F*-91128 *Palaiseau, France*

Accepted 2016 April 13. Received 2016 April 8; in original form 2015 October 2

SUMMARY

Inelastic deformation can either occur with dilatancy or compaction, implying differences in porosity changes, failure and petrophysical properties. In this study, the roles of water as a pore fluid, and of temperature, on the deformation and failure of a micritic limestone (white Tavel limestone, porosity 14.7 per cent) were investigated under triaxial stresses. For each sample, a hydrostatic load was applied up to the desired confining pressure (from 0 up to 85 MPa) at either room temperature or at 70 °C. Two pore fluid conditions were investigated at room temperature: dry and water saturated. The samples were deformed up to failure at a constant strain rate of $\sim 10^{-5}$ s^{-1}. The experiments were coupled with ultrasonic wave velocity surveys to monitor crack densities. The linear trend between the axial crack density and the relative volumetric strain beyond the onset of dilatancy suggests that cracks propagate at constant aspect ratio. The decrease of ultrasonic wave velocities beyond the onset of inelastic compaction in the semi-brittle regime indicates the ongoing interplay of shear-enhanced compaction and crack development. Water has a weakening effect on the onset of dilatancy in the brittle regime, but no measurable influence on the peak strength. Temperature lowers the confining pressure at which the brittle–semi-brittle transition is observed but does not change the stress states at the onset of inelastic compaction and at the post-yield onset of dilatancy.

Key words: Microstructures; Plasticity, diffusion, and creep; Elasticity and anelasticity; Fracture and flow.

1 INTRODUCTION

Human activities can lead to deformation and failure of porous rocks, for example during hydrocarbon exploitation because the pore pressure decreases, which leads to an increase of the effective stress, or in mines or underground storages, due to stress concentration. Many consequences are known: surface subsidence (e.g. Boutéca *et al.* 1996; Fredrich *et al.* 2000; Nagel 2001), well bore failure (e.g. Peška & Zoback 1995), induced seismicity (e.g. Talwani & Acree 1984; Simpson *et al.* 1988; Segall 1989) and permeability changes (e.g. David *et al.* 1994; Miller 2002; Bemer & Lombard 2010). These consequences may impact hydrocarbon or geothermal exploitation, as well as underground storage.

Limestones are one of the main groups of sedimentary rocks. They host a significant portion of the oil reserves (e.g. Murray 1930; Shariatpanahi *et al.* 2010), represent 7 per cent of land surfaces (e.g. Scholle *et al.* 1983), are used as an industrial material and have been proposed as reservoirs for the geological sequestration of carbon dioxide. At field scale, elastic wave velocities may be used to monitor changes in elastic properties, possible indicators of irreversible damage (4-D seismic). However, these changes are not straightforward to interpret (Hexsel Grochau *et al.* 2014).

Limestone failure modes depend on their initial porosity and change with applied effective stress (e.g. Wong & Baud 2012; Ji *et al.* 2015). Deformation can either be coupled with dilatancy, leading to shear localization and therefore brittle failure (Brace 1978; Paterson & Wong 2005), or result from microscopic plastic flow that does not involve any volumetric change (Paterson 1978). It has been known for a long time that calcite deforms by processes such as mechanical twinning or r-, f- dislocation glide at room temperature (Turner *et al.* 1954; Griggs *et al.* 1960; De Bresser & Spiers 1997). The induced brittle-ductile transition is of special interest for porous rocks, because it could provide some insight into fault mechanics and shallow earthquakes (Sibson 1982; Rutter 1986). The brittle-ductile transition in carbonate rocks is relatively easy to achieve in experiments because it is accessible at room temperature for confining pressures attainable in the laboratory (e.g. Robertson 1955; Paterson 1958; Heard 1960; Rutter 1972, 1974). Previous studies have already focused on limestones [e.g. Solnhofen limestone: Robertson (1955), Heard (1960), Rutter (1972, 1974), Hugman & Friedman (1979), Baud *et al.* (2000a); Tavel limestone: Vajdova *et al.* (2004, 2010); Indiana limestone: Vajdova *et al.* (2012); Majella limestone: Baud *et al.* (2009), Vajdova *et al.* (2012); Estaillades limestone: Dautriat *et al.* (2011a,b)] and marbles [e.g. Carrara marble: Rutter

(1972, 1974), Fredrich *et al.* (1989), Schubnel *et al.* (2006); Yule marble: Hugman & Friedman (1979)].

Dilatancy and plastic flows can combine their effects, leading to transitional behaviour named cataclastic flow, characterized by homogeneously-distributed microcracking, grain rotations and grain plasticity (twinning and dislocations), as discussed by Fredrich *et al.* (1989). Cataclastic flow can either lead to dilatancy as shown by Fredrich *et al.* (1989) on a very low porosity Carrara marble or to inelastic compaction as observed by Baud *et al.* (2000a), Vajdova *et al.* (2004), Vajdova *et al.* (2010) and Wong & Baud (2012) on limestones and chalks of various porosities. However, compactive cataclastic flow is commonly observed to be a transient phenomenon. Indeed the failure mode evolves with increasing strain to dilatant cataclastic flow and ultimately shear localization (Baud *et al.* 2000a).

Initial porosity is a key parameter that controls the deformation and failure modes of limestones (Vajdova *et al.* 2004). Dautriat *et al.* (2011a) showed that structural heterogeneities can influence the localization of damage, and Zhu *et al.* (2010) and Regnet *et al.* (2015a) showed that the microporosity distribution also plays a role. Pore fluid and temperature are also important parameters (Rutter 1972, 1974). Water generally reduces the brittle strength, as a result of adsorption: water as a pore fluid decreases the surface energy, promotes subcritical crack growth and stress corrosion (Clarke *et al.* 1986; Atkinson & Meredith 1987; Costin 1987; Baud *et al.* 2000b; Risnes *et al.* 2005; Røyne *et al.* 2011; Liteanu *et al.* 2013), which can have effects on co-seismic sliding friction (Violay *et al.* 2013). Temperature modifies the short-term strength and time-dependent creep behaviour of sandstones (Heap *et al.* 2009), and is likely to have the same effects on limestones. As pore fluid and temperature may vary in natural conditions, the study of the deformation and failure modes should be performed under varying P–T conditions in dry and water-saturated samples.

This study focuses on the mechanical behaviour of a limestone with an initial porosity of 14.7 per cent. The question we address is: How do temperature and the presence of water as a pore fluid influence the deformation mechanisms? We report results of conventional triaxial experiments performed at various confining pressures in the range of 0–100 MPa, at 20 °C under dry and water-saturated conditions, and at 70 °C under dry conditions. During these experiments, evolution of P- and S- wave velocities were measured. As shown by several authors (e.g. Fortin *et al.* 2005; Schubnel *et al.* 2006; Benson *et al.* 2006; Fortin *et al.* 2007; Regnet *et al.* 2015b), their evolution is very sensitive to the presence of microcracks, which makes them a good tool to track the evolution of irreversible damage.

2 MATERIAL AND METHODS

2.1 Rock material and sample preparation

Experiments shown in this paper were performed on white Tavel, a micritic and microporous limestone. This rock is mainly composed of coarse grained micrite particles (mean diameter ∼5 μm) cemented together, leading to larger micritic aggregates

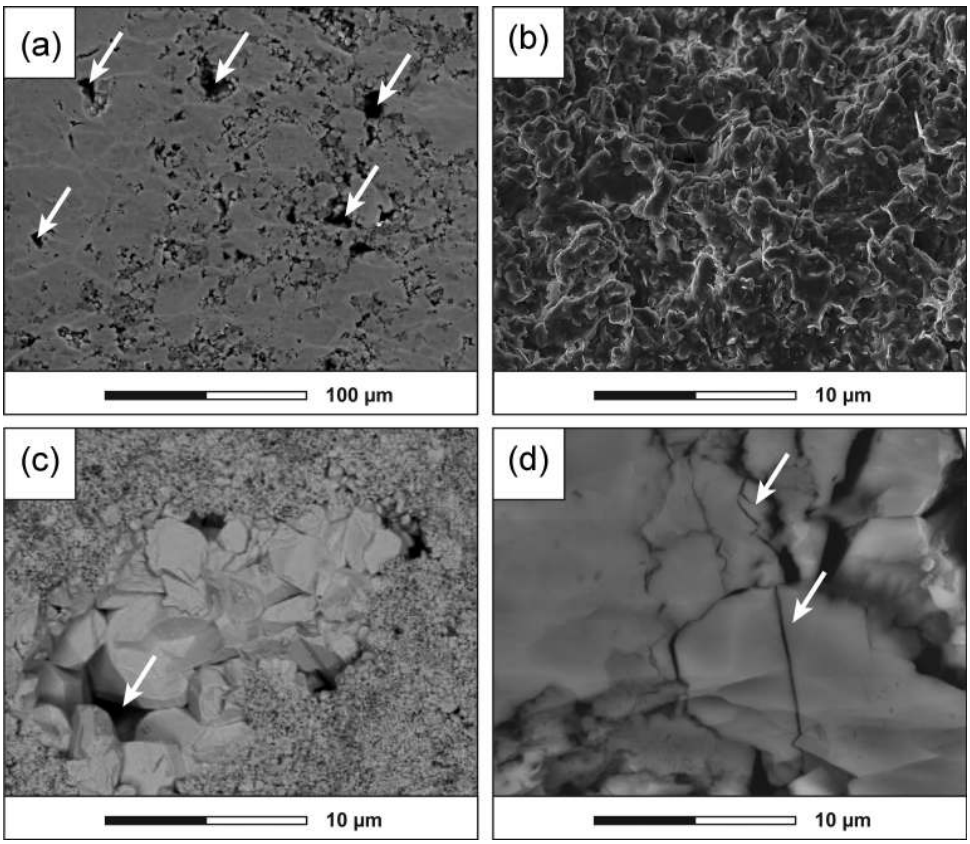

Figure 1. Micrographs of Tavel Limestone in Scanning Electron Microscope. (a) General observations of the layout. Larger micropores (white arrows) can be observed between or within micritic aggregates. (b) Micritic aggregate composed of coarse anhedral micrite particles (≥ 4 μm) with fused to indistinct contacts. (c) Incomplete sparitic cementation in a pre-existing bioclast, at the origin of larger micropores (white arrow). (d) Micritic aggregate observed on an ion-beam polished thin section. Initial crack porosity can be observed (regular or wing cracks, white arrows).

(Figs 1a and b). In this general micritic layout, some larger micropores (diameter between 2 μm and 10 μm) can be observed in sparitic parts, where cementation or recrystallization of pre-existing bioclasts is incomplete (Figs 1a and c). A more detailed observation on ion-beam polished thin-sections reveals the presence of a low initial crack porosity, located between micritic aggregates and/or micrite particles (Fig. 1d).

This limestone was used in previous studies by Vincké *et al.* (1998) and Vajdova *et al.* (2004, 2010). Scanning electron microscope (SEM) investigation showed that the composition of this Tavel limestone is almost 99 per cent calcite, in good agreement with Vajdova *et al.* (2004) who measured a composition of more than 98 per cent calcite. All samples were cored in the same block, and thin sections have been made in several samples, allowing us to have a robust control on the microstructure, avoiding heterogeneous samples. Thin sections were impregnated with blue-dyed epoxy to visualize the pore space.

Average porosity is 14.7 per cent, with maximum porosity variations of about 0.5 per cent around the average value. Porosity values were obtained from two measurements: (1) using the density of dried samples and assuming a 100 per cent calcite matrix composition and (2) using a triple weight procedure. The porosity is higher than that of Vajdova *et al.*'s samples, which was found to be 10.4 per cent. Note that the two sets of samples are from the same quarry (Tavel, France).

No obvious bedding is identified but all samples were cored parallel to avoid any problem of preferential direction. The isotropy of the rock is examined later in the article. The diameter of our cylindrical samples is 40 mm and their length is 86 mm. After coring, faces are ground to ensure a good parallelism. Strain gauges (*Tokyo Sokki TML* type FCB 2-11 for experiments at room temperature and *Tokyo Sokki TML* type QFCB 2-11 for experiments at higher temperature) are directly glued onto the sample surface. These gauges are each composed of one axial and one radial gauge. Neoprene tubing is used to separate the sample from oil confining medium. Before an experiment, samples are dried in an oven at ∼40 °C for several days.

2.2 Experimental apparatus

The pressure vessel used in this study is a conventional triaxial cell installed in the Laboratoire de Géologie at the École Normale Supérieure in Paris. A detailed description of the apparatus can be found in Brantut *et al.* (2011); Ougier-Simonin *et al.* (2011). In this paper, compressive stresses and compactive strains are counted positive. The principal stresses will be denoted σ_1 and σ_3, σ_1 being the highest principal stress and σ_3 the confining pressure. The differential stress $\sigma_1 - \sigma_3$ will be denoted Q and the mean stress $(\sigma_1 + 2\sigma_3)/3$ will be denoted P. The confining pressure ($\sigma_2 = \sigma_3$) is measured by a pressure transducer with an accuracy of about 10^{-2} MPa. Effective pressure is calculated as $P_{\text{eff}} = P - P_{\text{pore}}$, P_{eff} being the effective pressure, and P_{pore} the pore pressure. The effective confining pressure is calculated as $\sigma_{3,\text{eff}} = \sigma_3 - P_{\text{pore}}$, where σ_3 is the confining pressure. Axial load is applied by an axial piston, and is measured with an accuracy of about 10^{-2} MPa. The axial displacement is measured with four axial strain gauges and three displacement transducers (DCDT) mounted outside the pressure vessel between the moving piston and the fixed lower platen. For both strain gauges and DCDTs, we consider mean displacements. The DCDT measurements are corrected for the stiffness of the cell using the strain gauge measurements. We do not use the axial strain gauges excepted for DCDT measurement correction because under large strains ($\varepsilon_{ax} \geq 2$ per cent) attainable with carbonate rocks, strain gauges break, whereas DCDTs have no strain limitation. Radial strains are measured with four radial strain gauges. Radial gauges are used because they undergo much smaller strains that axial strain gauges. Uncertainty in strain measured with gauges is estimated to be of the order of 10^{-5}; and DCDT signals have an accuracy of about 10^{-4}.

The volumetric strain is calculated as $\varepsilon_v = \varepsilon_{ax} + 2\varepsilon_r$, where ε_{ax} and ε_r are the axial and radial strains, respectively. This formula neglects second-order contributions of strains to the volume change that may be appreciable at relatively large strains. For water-saturated experiments, pore pressure can be controlled at the top and the bottom of the sample with two microvolumetric pumps (Quizix) with an accuracy of about 10^{-2} MPa.

For experiments performed at 20 °C, temperature is controlled by air conditioning. For experiments performed at 70 °C, the triaxial cell is equipped with a heating system. The maximum heating rate is approximately 1 °C min^{-1}. The temperature inside the vessel is recorded via two thermo-couples, one being plunged in the confining oil and the other touching the bottom end of the lower steel plug.

2.3 Ultrasonic wave velocities

Eight piezoelectric transducers (PZTs) were directly glued onto the sample surface. We used four PZT sensors sensitive to *P*-waves and four sensitive to *S*-waves. Both types of PZT sensors have a resonant frequency around 1 MHz. The small number of PZT sensors does not allow us to locate acoustic emissions (AE). However, no significant AE activity was recorded. Therefore PZT sensors were only used to measure the evolution of *P*-wave and *S*-wave velocities during the experiment. Every 1 or 2 min during the experiment, a 250 V high frequency signal is pulsed on each sensor while the others are recording. The electrical signal received is amplified at 40 dB. A thorough description of the acoustic system can be found in Brantut *et al.* (2011). The position of each sensor is known and is corrected for the sample deformation during the experiment. *P*- or *S*-wave traveltime allows us to calculate the *P*-wave velocities at an angle of 90° and ∼53° with the axis of symmetry, as well as the horizontal *SH*- and vertical *SV*-wave velocities at an angle of 90° (Fig. 2). Arrival times are known with an accuracy of 0.1 μs, which leads to an accuracy on ultrasonic velocity of ∼5 per cent.

2.4 Experimental procedure

The 18 complete and 11 partial triaxial experiments were performed at effective confining pressures ranging from 0 MPa (uniaxial experiment) to 85 MPa. A set of experiments was conducted at 20 °C in dry and water saturated conditions and in dry conditions at 70 °C. Experimental conditions of each experiment (confining pressure, pore fluid and temperature) can be found in Tables 1 and 2.

Samples deformed in dry conditions at 20 °C were first loaded isostatically up to the desired confining pressure. The differential stress is then applied by deforming the sample at a controlled strain rate of $\sim 10^{-5}$ s^{-1}. Concerning experiments conducted in dry conditions at 70 °C, the dry sample is first loaded isostatically up to a pressure of 20 MPa. Confining pressure is kept constant at 20 MPa during heating (∼18 hr). The temperature is considered to be homogeneous when the difference between the two

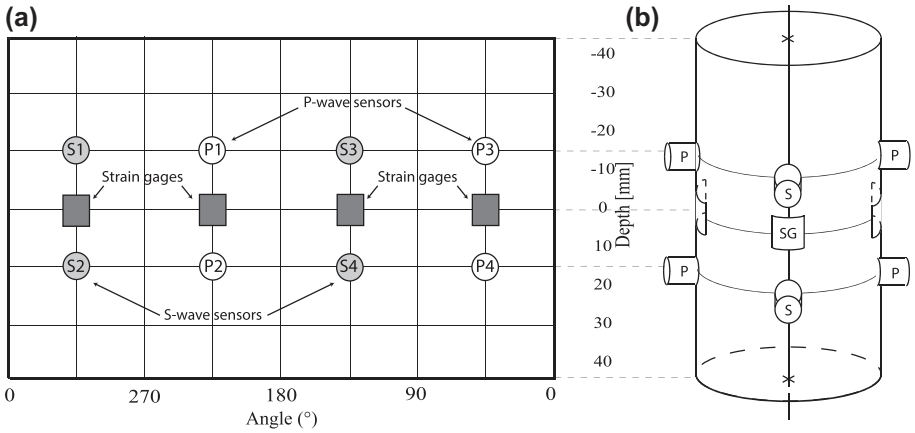

Figure 2. (a) Sensor map used for the experiments. Ultrasonic wave velocities (*P* and *S*) were measured on directions forming an angle of 53° and 90° with the sample axis. A schematic view of a prepared sample is given in panel (b).

Table 1. Summary of the mechanical data obtained on white Tavel limestone and presented in Fig. 4. This table gives effective mean stresses for the onset of dilatancy (C'), onset of inelastic compaction (C^*), post-yield onset of dilatancy ($C^{*\prime}$) and peak stresses.

No.	Pore fluid	P_{eff} (MPa)	P_p (MPa)	Temperature (°C)	C' (MPa)	C^* (MPa)	$C^{*\prime}$[a] (MPa)	Peak stress[a] (MPa)	ϕ[b] (°)
1	dry	0	0	20	20 ± 5	–	–	32	–
2	dry	20	0	20	56 ± 5	–	–	77.4	16
3	dry	35	0	20	80 ± 7.5	–	–	114.3	25
4	dry	55	0	20	105 ± 10	–	–	136.7	30
5	dry	70	0	20	–	117 ± 7.5	161.3	–	29
6	dry	85	0	20	–	134 ± 7.5	181.5	–	–
7	dry	85	0	20	–	133 ± 7.5	174	–	–
8	water	20	5	20	45 ± 10	–	–	87.5	19
9	water	35	5	20	63 ± 5	–	–	103.1	28
10	water	55	5	20	94 ± 10	–	–	141.6	29
11	water	70	5	20	–	126 ± 7.5	161.8	–	–
12	water	85	5	20	–	134 ± 10	178.3	–	–
13	dry	5	0	70	28 ± 7.5	–	–	55	–
14	dry	20	0	70	55 ± 5	–	–	74.5	21
15	dry	35	0	70	82 ± 5	–	–	101.8	20
16	dry	55	0	70	–	106 ± 10	140.6	–	19
17	dry	70	0	70	–	118 ± 10	152.7	–	25
18	dry	85	0	70	–	131 ± 10	173	–	–

[a]Uncertainty is less than 0.2 MPa for these stress states.
[b]ϕ corresponds to the angle between the vertical axis and the macroscopic fault trace in the sample.

Table 2. Summary of the additional mechanical data obtained on white Tavel limestone. These samples were not deformed up to failure, thus these data are not reported in Fig. 4 but they are presented in Appendix C (Fig. C1). However, from these experiments it is possible to get effective mean stresses for the onset of dilatancy (C'), onset of inelastic compaction (C^*) and for one experiment post-yield onset of dilatancy ($C^{*\prime}$).

No.	Pore fluid	P_{eff} (MPa)	P_p (MPa)	C' (MPa)	C^* (MPa)	$C^{*\prime}$[a] (MPa)	Peak stress[a] (MPa)
1	dry	20	0	58 ± 5	–	–	–
2	dry	35	0	78 ± 5	–	–	–
3	dry	55	0	95 ± 7.5	–	–	–
4	dry	70	0	–	121 ± 5	158	–
5	dry	70	0	–	120 ± 5	–	–
6	dry	85	0	–	132 ± 5	–	–
7	dry	85	0	–	135 ± 5	–	–
8	water	20	5	48 ± 5	–	–	–
9	water	35	5	62 ± 5	–	–	–
10	water	55	5	88 ± 5	–	–	–
11	water	85	5	–	120 ± 5	–	–

[a]Uncertainty is less than 0.2 MPa for these stress states.

thermo-couples is lower than 1 °C. At that point, the procedure becomes similar to that for dry samples at room temperature.

For water-saturated experiments, the dry sample is loaded isostatically up to a pressure of 20 MPa and saturated with water at equilibrium with calcite. Saturation is controlled with the micro-volumetric pumps. Full saturation is assumed to be reached when the total injected volume of water is stable. At that point, a pressure difference of 1 MPa is applied between the bottom and the top of the sample during ∼30 min in order to flush the air trapped within the sample. Then, the pore pressure is maintained constant at a pressure of 5 MPa during all the experiment and the procedure becomes similar to that for dry samples.

2.5 Are water-saturated experiments performed under drained conditions?

The hydromechanical behaviour of a permeable rock is directly related to the condition of drainage during deformation (e.g. Guéguen & Boutéca 1999; Duda & Renner 2013). A key point before conducting water-saturated experiments is to check whether the conditions are drained or not. Characteristic time t for diffusion over a distance l (to get fluid pressure equilibrium) can be approximated by (Carslaw & Jaeger 1959; Ge & Stover 2000; Duda & Renner 2013):

$$t \sim \frac{l^2}{D}, \tag{1}$$

where D is the hydraulic diffusivity. The hydraulic diffusivity D can be approximated by (Kümpel 1991):

$$D \sim \frac{kBK_d}{\eta\alpha}, \tag{2}$$

where k is the permeability, B is Skempton's coefficient, K_d is the drained bulk modulus, η is the fluid viscosity, and α is Biot's coefficient. For white Tavel limestone and water, $k = 10^{-16}$ m^2, $\eta = 1.002 \times 10^{-3}$ Pa s, and $K_d = 27$ GPa. Assuming that Skempton's coefficient and Biot's coefficient to be of the order of unity, one obtains $D \sim 2.7\,10^{-3}$ m^2 s^{-1}. For $l = 4$ cm (half length of the sample), one gets $t \sim 1$ s, which is a short time compared to that of our experiments (between 10 min and 1 h). Thus, our experiments can be considered as conducted in drained conditions.

3 RESULTS

3.1 Mechanical behaviour during isostatic loading

Results for a hydrostatic loading experiment with up to 85 MPa confining pressure performed on a dry sample at a temperature of 20 °C are presented in Fig. 3. Fig. 3(c) is discussed later in the article. The hydrostatic response was non-linear up to a pressure of ∼52 MPa, beyond which the stress-strain curve became linear with a slope corresponding to a static bulk modulus (or 'deformation-derived modulus') of $K = 26.7$ GPa (Fig. 3a). The nonlinearity observed below 52 MPa can be explained by the progressive closure of pre-existing microcracks (Baud *et al.* 2000a; Vajdova *et al.* 2004), such as the one present in Fig. 1(a). Comparing the volumetric strain measured and the perfectly elastic trend, microcrack porosity can be estimated to be ∼0.07 per cent (Walsh 1965).

As pressure is increased from 0 to 52 MPa, ultrasonic P and S wave velocities increase from 4135 m s^{-1} and 2200 m s^{-1} to 4350 m s^{-1} and 2350 m s^{-1}, respectively (Fig. 3b). Together with the static measurements, this increase highlights the closure of pre-existing cracks (e.g. Fortin *et al.* 2005) between 0 and 52 MPa. Above 52 MPa, P and S wave velocities remain constant at 4350 m s^{-1} and 2350 m s^{-1}, respectively. This observation suggests that all cracks are closed above 52 MPa, in agreement with the linear stress-strain relation. Using ultrasonic wave velocities at isostatic pressure above 52 MPa and relations between dynamic elastic (or 'linear elastic derived') moduli and ultrasonic wave propagation velocities, the dynamic bulk modulus K_0 is found to be $K_0 = 26.9$ GPa. Under isostatic stress conditions, our results show that ultrasonic wave velocities are independent from their pathway, indicating that the medium composed of matrix with embedded pores and cracks is isotropic.

3.2 Mechanical behaviour during deviatoric loading

The mechanical behaviour observed during experiments conducted on dry samples at 20 °C depend upon the confining pressure (Figs 4a and d). For P_c lower than 55 MPa, the mechanical behaviour and failure mode are typical of the brittle faulting regime: The axial strain versus differential stress curves first show a linear trend typical of an elastic behaviour (Fig. 4a). Then, the differential

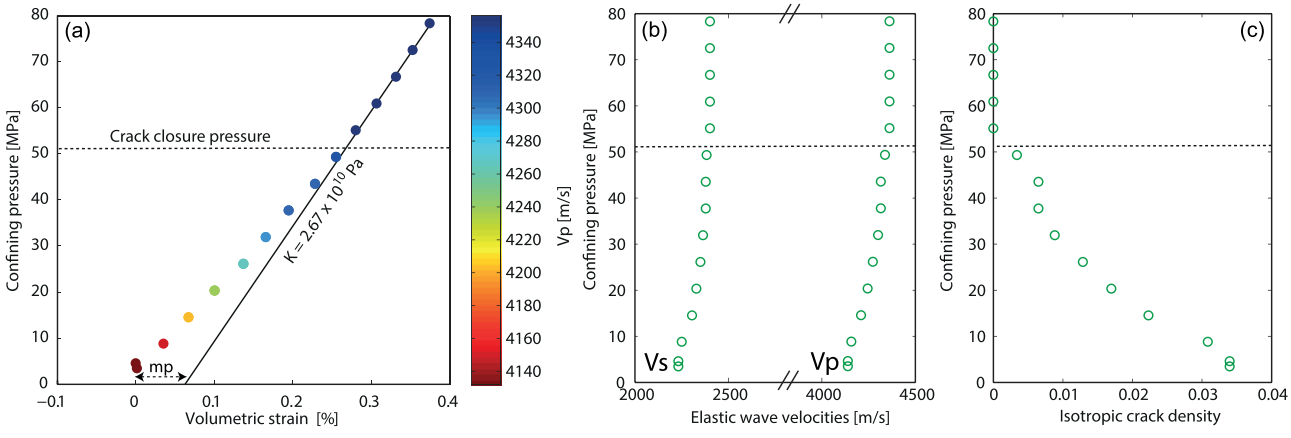

Figure 3. (a) Evolution of the volumetric strain plotted versus confining pressure. The colour of the points are related to the P-wave velocities measured during the loading. The black line corresponds to a linear elastic behaviour for a static bulk modulus of 26.7 GPa. The dashed line corresponds to the crack closure pressure inferred from the volumetric strain. The microcrack porosity is shown by an arrow labelled *mp* on the figure. (b) Evolution of the ultrasonic wave velocities plotted against the confining pressure. The dashed line corresponds to the crack closure pressure inferred from panel (a). (c) Evolution of the isotropic crack density plotted against the confining pressure. The dashed line corresponds to the crack closure pressure inferred from panel (a).

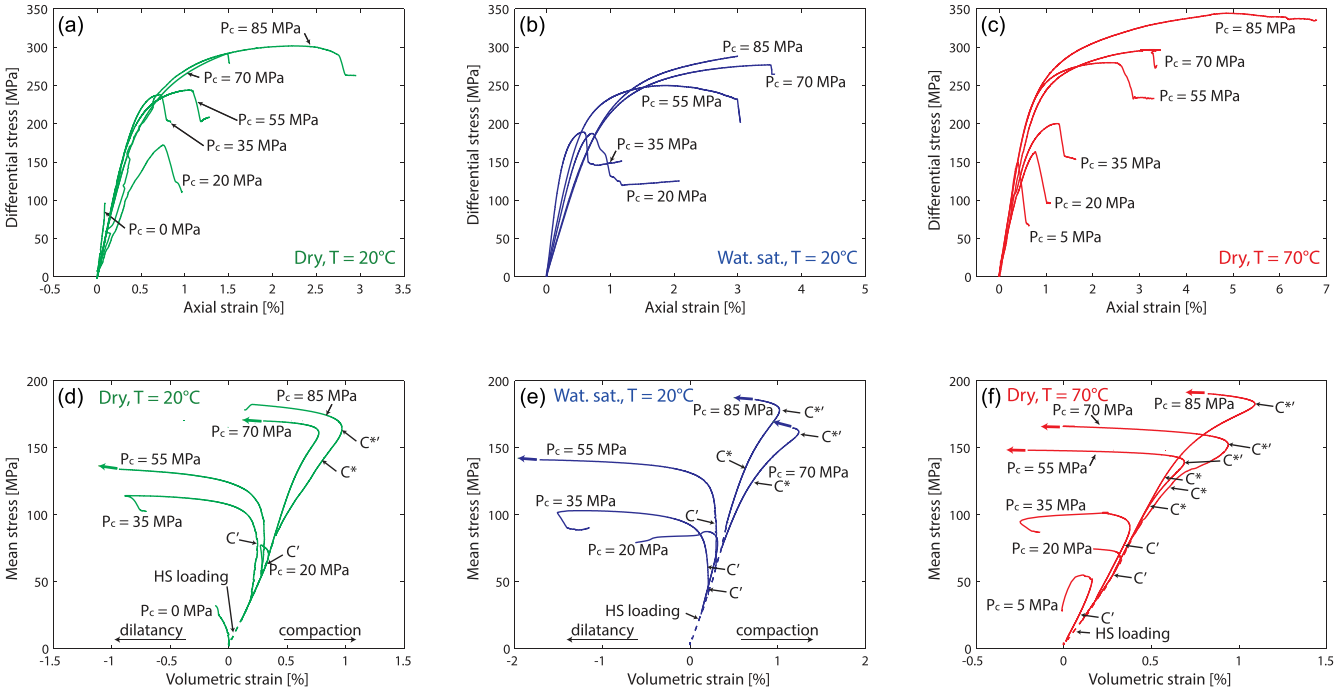

Figure 4. Compilation of mechanical data for complete experiments. The differential stress is plotted versus axial strain for experiments on (a) dry samples at 20 °C, (b) water-saturated samples at 20 °C, and (c) dry samples at 70 °C. The mean stress versus volumetric strain curves for these three sets of experiments are shown in panels (d)–(f). Stress states at the onset of dilatancy C', onset of inelastic compaction C^* and post-yield onset of dilatancy $C^{*\prime}$ are shown for references on some experiments. Note that the radial strain gages broke at strains larger than 1 per cent, so that the last part of these plots are missing and symbolized by an arrow.

stress reaches a peak, beyond which strain softening is taking place (Fig. 4a). From the volumetric strain versus mean stress curves (Fig. 4d), it can be seen that samples show an elastic compactant behaviour until a critical stress state denoted C' (Wong *et al.* 1997) beyond which the volumetric strain deviates from linear elasticity (onset of dilatancy). The critical stress state C' is determined manually at the point of divergence of the curve of volumetric strain versus mean stress and the linear elastic compaction of each experiment. To our knowledge, no previous article has reported error bars for the onset of dilatancy, which remains somehow subjective. The error bar given for each critical stress in this article (Tables 1 and 2 and Fig. 5) corresponds to an upper bound and account for the subjective part of the critical stress determination. Note that although error bars are wide, results remain well reproducible (Tables 1 and 2). The differential stress levels at the onset of dilatancy (C') and peak stress show a positive confining pressure dependence (Fig. 4 and Tables 1 and 2).

For P_c equal or higher than 70 MPa, the mechanical behaviour is different from the one at lower pressures and is characterized by three different stages: a compactive elastic behaviour, beyond which an inelastic compactive regime takes place. The transition between these two domains is characterized by the stress C^* (Wong *et al.* 1997). The critical stress state C^* is determined manually at the point of divergence of the curve of volumetric strain versus mean stress and the linear elastic compaction of each experiment. This inelastic compaction is characterized by a decrease in volume larger than the elastic one and is referred to as shear-enhanced compaction (Wong *et al.* 1992, 1997). In these experiments, inelastic compaction is a transient phenomenon. Indeed, the volumetric strain evolves with increasing strain to dilatant cataclastic flow beyond a critical state denoted $C^{*\prime}$ (Wong *et al.* 1997). Between the onset of inelastic compaction (stress state C^*) and the post-yield onset of dilatancy (stress state $C^{*\prime}$), compaction and dilatancy are likely to take place simultaneously (e.g. Edmond & Paterson 1972; Dresen & Evans 1993) but compaction is dominant. At $C^{*\prime}$, dilatancy overcomes compaction. The critical stresses at the onset of post-yield dilatancy ($C^{*\prime}$) exhibit a positive dependence on confining pressure (Fig. 5a). Relying on our experiments, the lack of data make it impossible to conclude about a possible pressure dependence of the stress state at the onset of inelastic compaction (C^*), although it is known that C^* has a negative pressure dependence (Baud *et al.* 2000a). The mechanical behaviour observed for P_c equal or higher than 70 MPa can be considered as semi-brittle as defined by Evans *et al.* (1990). The semi-brittle regime is characterized by macroscopically distributed deformation involving crystal plasticity and microcracking (Evans *et al.* 1990). Comparing the volumetric strain versus mean stress of all samples, the brittle–semi-brittle transition occurs at a confining pressure between 55 MPa and 70 MPa, under dry conditions at 20 °C.

In water-saturated conditions, the mechanical behaviour is very similar to that observed in dry experiments. For P_c lower than 55 MPa, the mechanical response and failure mode are typical of the brittle faulting regime, showing dilatancy and strain softening (Figs 4b and e). For P_c equal to, or higher than, 70 MPa, the mechanical behaviour clearly shows an inelastic compaction identified as shear-enhanced compaction, which induces strain hardening but ultimately switches from shear-enhanced compaction to dilatancy (Figs 4b and e). Water has a weakening effect in the brittle regime: stresses at the onset of dilatancy (C') in water-saturated experiments are lower than that obtained in dry experiments (Fig. 5a). However, no clear effect is recorded (1) on the peak strength, (2) on the stress state at the onset of inelastic compaction (C^*) and (3) on the stress state at the post-yield onset of dilatancy ($C^{*\prime}$). The brittle–semi-brittle transition is occurring at a confining between 55 MPa and

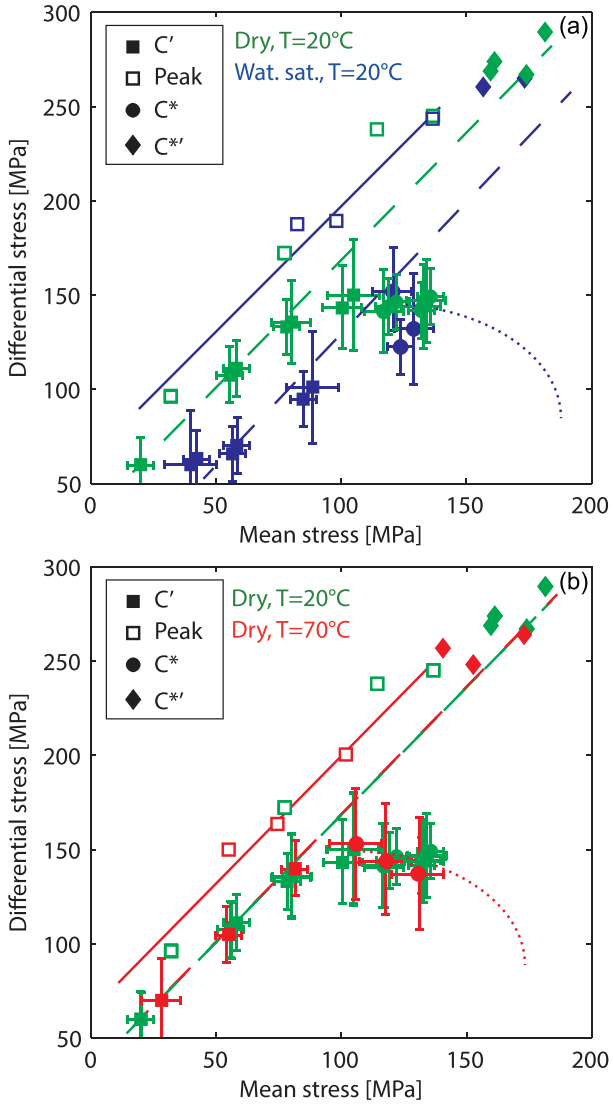

Figure 5. Peak stress (empty squares), and thresholds C' (plain squares), C^* (plain dots) and $C^{*\prime}$ (plain diamonds) from Tables 1 and 2 are shown in the P–Q space for (a) dry samples at 20 °C (green) and water-saturated samples at 20 °C (blue), and (b) dry samples at 20 °C (green) and dry samples at 70 °C (red).

70 MPa, at similar values than those obtained for dry conditions.

The behaviour observed during the experiments performed in dry conditions at 70 °C is qualitatively similar to the previous ones. At 5 and 35 MPa confining pressure, the mechanical response and failure mode are typical of the brittle faulting regime (Figs 4c and f). For P_c higher than 55 MPa, the mechanical behaviour shows shear-enhanced compaction, which ultimately switches to dilatancy. Stresses at the onset of dilatancy (C'), onset of inelastic compaction (C^*), onset of post-yield dilatancy ($C^{*\prime}$) and peak stress are identical for experiments performed at $T = 20$ °C and $T = 70$ °C in dry conditions (Fig. 5b). However, the brittle–semi-brittle transition occurs for a confinement between 35 and 55 MPa, a lower value than that obtained at room temperature (between 55 and 70 MPa; Fig. 5b). At $T = 20$ °C, the experiment performed at a confining pressure of 55 MPa clearly exhibits a brittle behaviour, whereas the one performed at the same confinement but at $T = 70$ °C shows shear-enhanced compaction (Fig. 6).

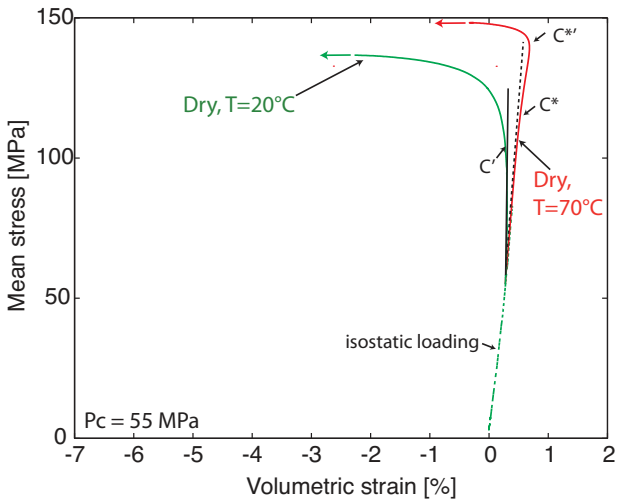

Figure 6. Volumetric strain versus mean stress for experiments performed in dry conditions at a confining pressure of 55 MPa at 20 and 70 °C. At 20 °C, the mechanical response is typical of the brittle faulting regime, whereas the mechanical response at 70 °C shows inelastic compaction typical of the semi-brittle regime.

3.3 Post-mortem microstructural analysis

Samples were unloaded and retrieved from the pressure vessel at the end of the experiments. The deformed samples were first impregnated with epoxy and then sawed along a plane parallel to the axial direction to prepare petrographic thin sections. To characterize deformation-related features in the most detailed way, SEM was used. Fig. 7 presents a selection of pictures for samples deformed at $P_c = 20$ MPa and $P_c = 85$ MPa, which illustrate the two observed mechanical behaviours (brittle and semi-brittle, respectively).

Samples of the brittle fracture regime are characterized by the localization of deformation on a low-angle shear fracture (∼30°) (Fig. 7a). Microcracking seems to be the dominant mechanism of dilatant failure in brittle faulting in Tavel Limestone, although a very low twinning activity was also observed. Observations show a complex fracture and crack network mainly developed in micritic parts, but also in sparite crystals (Figs 7b and c). Those deformation-related fractures/cracks are coloured and highlighted by the blue-dyed epoxy, and account for a non-negligible porosity creation, especially when considering the displacement on the main shear fracture (Fig. 7d). Overall, those features are characteristic of the brittle fault regime, and in good agreement with the observed mechanical behaviour.

Samples of the semi-brittle fracture regime (ductile type of behaviour) show no localization of the deformation but a slight barrel shape after the experiment (Fig. 7e). Microscopic observations reveal an intense twinning activity within the sparite crystals (Fig. 7f) which appears to be an important deformation mechanism in those samples. This twinning activity is often coupled with grain-crushing (Fig. 7g) and non-coalescent microcracks within sparite crystals (Fig. 7h). Those stress-induced cracks are preferentially aligned and propagated subparallel to σ_1. Those features are in good agreement with deformation mechanism found in the semi-brittle regime.

3.4 Evolution of ultrasonic wave velocities during triaxial loading

During the initial stage of elastic loading, no variation of velocities is recorded for experiments performed at $P_c \geq 55$ MPa, neither for

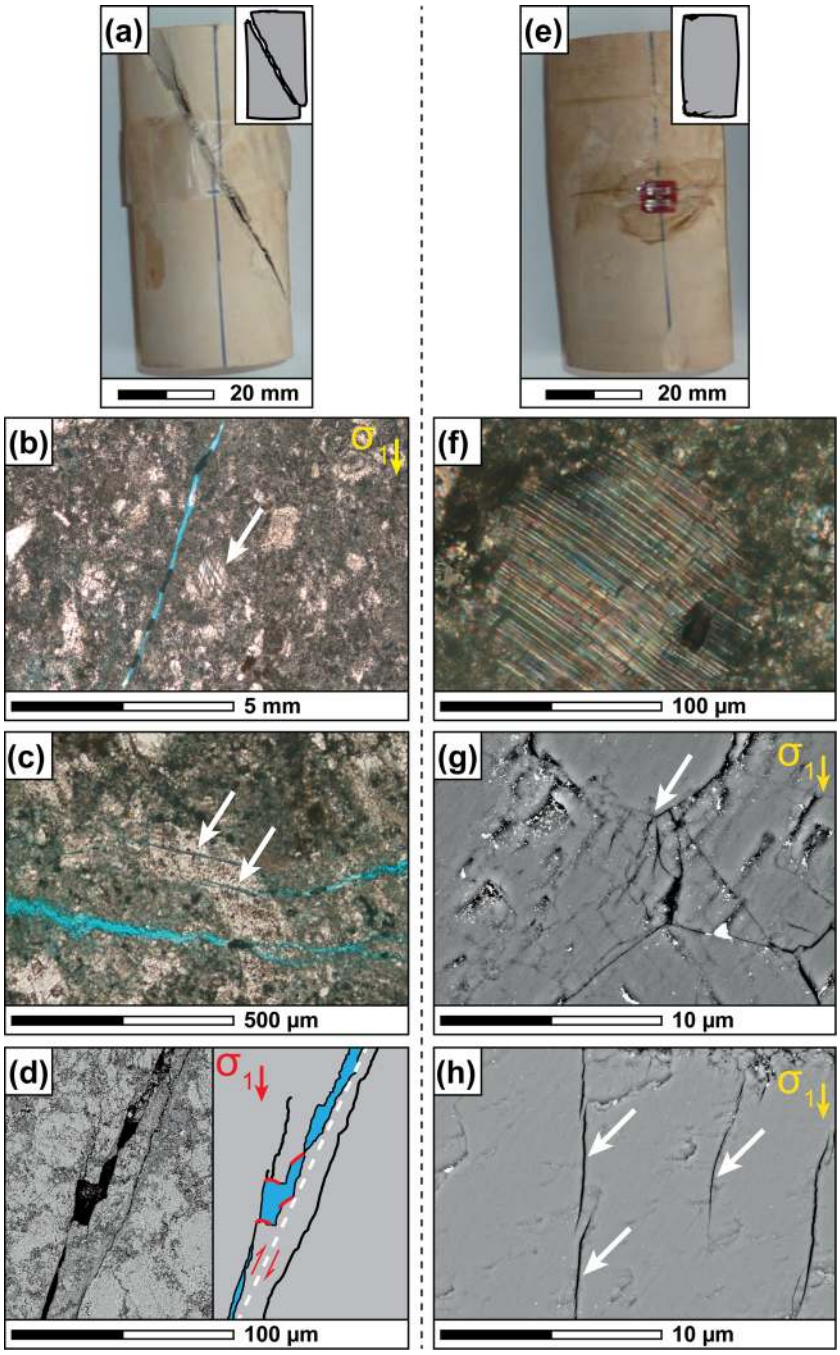

Figure 7. Pictures and micrographs of two samples characterized by brittle (a–d) and semi-brittle (e–h) behaviours after unloading (optical microscopy and SEM). (a) Deformation localization on a shear fracture for the sample deformed at $P_c = 20$ MPa. (b) Shear fracture under optical microscopy (blue-coloured) that propagated in the micritic part of the rock. Note the low twinning activity in the sparite crystal (white arrow), associated with intragranular cracks. (c) Stress-induced fracture and crack network in micrite and sparite, respectively (white arrows). (d) Displacement on the main fracture, leading to porosity creation. (e) A stress-induced barrel-shape is observed after deformation for the sample deformed at $P_c = 85$ MPa. (f) Intense twinning activity in a sparite. (g) Grain-crushing phenomenon between two large sparites. Cracks propagate subparallel to σ_1. (h) Wing cracks in a large sparite, subparallel to σ_1. Those cracks do not coalesce from one to another.

P-waves nor for *S*-waves (Figs 8 and 9). Beyond the stage of elastic loading, variations of ultrasonic wave velocities depend upon the confining pressure.

In the brittle regime, that is, for P_c below 55 MPa for experiments performed at $T = 20\,^{\circ}$C and for P_c below 35 MPa for experiments performed at $T = 70\,^{\circ}$C, V_p and V_s start decreasing at the onset of dilatancy (C') (Figs 8c–f and 9c–f). Comparing the ultrasonic wave velocity decrease to the volumetric change (e.g. Fig. 10 for *P*-wave velocity), the decrease in velocities is sharper around the onset of dilatancy (C'). Just beyond C', velocities continue to decrease as the sample is deformed until failure. The overall decrease for both V_p and V_s reaches 25 per cent to 30 per cent for all the experiments. The same features are observed in water-saturated conditions and at $T = 70\,^{\circ}$C (Figs 8d–f and 9d–f).

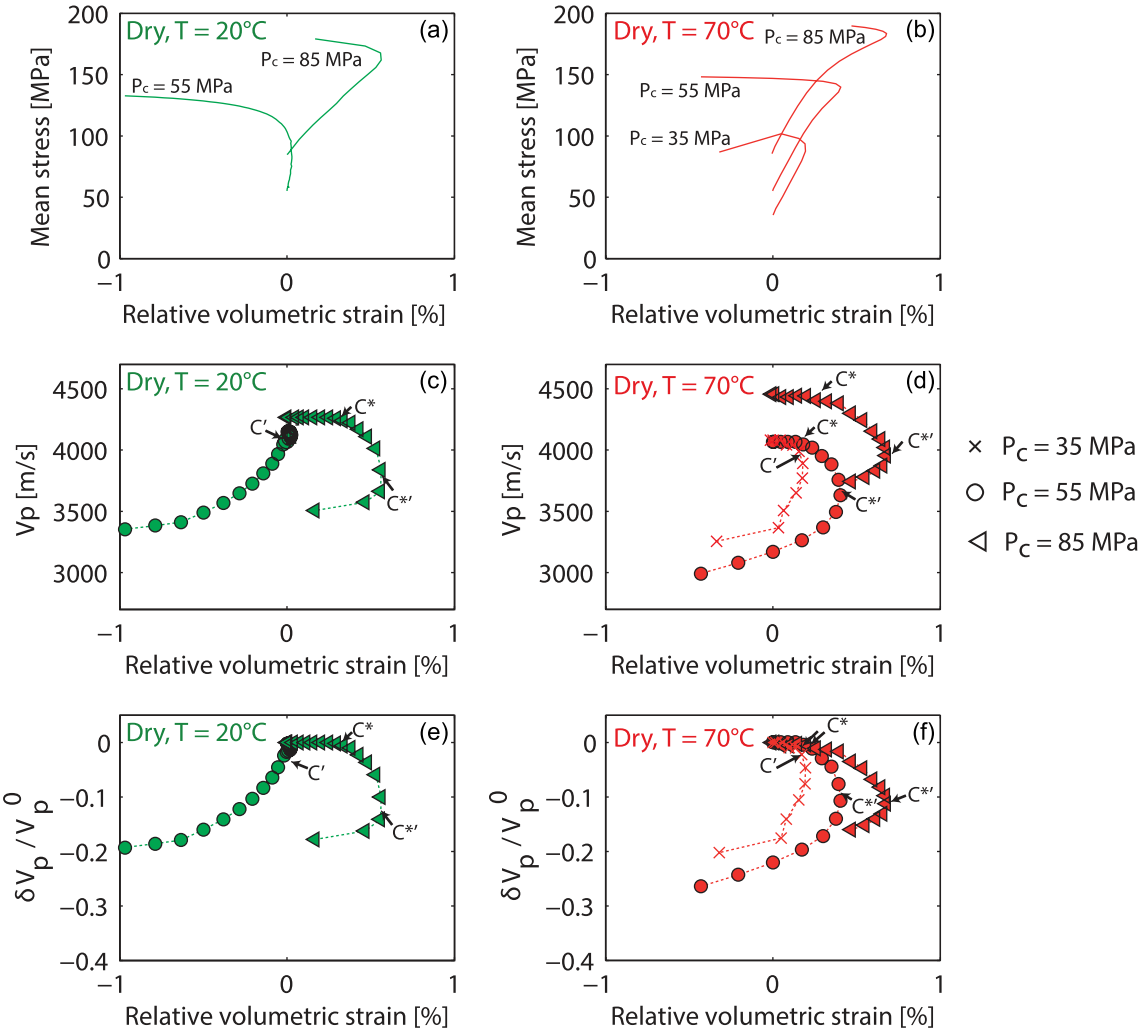

Figure 8. Compilation of mechanical and *P*-waves data for selected experiments. Note that strains are 'relative strains', that is, the zero strain is that at the end of the hydrostatic loading. Relative volumetric strain versus mean stress is shown for reference in (a) and (b) for dry experiments at 20 °C and dry experiments at 70 °C, respectively. (c) and (d) show the evolution of *P*-wave velocities perpendicular to σ_1 versus the relative volumetric strain for the two sets of experiments. (e) and (f) show the evolution of $\delta V_p / V_p^0$ versus relative volumetric strain, where V_p^0 is the *P*-wave velocity at the beginning of the triaxial loading.

In the semi-brittle regime, that is, for P_c above 55 MPa for experiments performed at $T = 20\,^{\circ}$C and for P_c above 35 MPa for experiments performed at $T = 70\,^{\circ}$C, the evolution of ultrasonic wave velocities is different than that observed in the brittle regime. In the elastic compaction stage, no change of V_p and V_s is measured (Figs 8c–f and 9c–f). Beyond the onset of inelastic compaction (C^*) ultrasonic wave velocities start to decrease, and the decrease rate accelerates as the post-yield onset of dilatancy ($C^{*\prime}$) is approached. At $C^{*\prime}$ V_p and V_s a decrease of 10 per cent to 20 per cent is observed. Around $C^{*\prime}$, the decrease of V_p and V_s as a function of the volumetric change is maximum (Fig. 10, experiment performed at $P_c = 85$ MPa). Beyond the post-yield onset of dilatancy $C^{*\prime}$, in the dilatancy stage, V_p and V_s continue to decrease down to values 30 per cent lower than their initial value (Figs 8c–f and 9c–f). For experiments performed at $T = 70\,^{\circ}$C, the decrease of ultrasonic wave velocities around $C^{*\prime}$ seems to be slightly less important than for experiments performed at $T = 20\,^{\circ}$C (Figs 8c–f and 9c–f). Finally, the evolution of ultrasonic wave velocities can be added to the mechanical data (Fig. 11) and is directly correlated to dilatancy.

4 DISCUSSION

4.1 From inverted crack density to macroscopic deformation at isostatic stress

The mechanical response of Tavel limestone subjected to isostatic loading (Fig. 3) is typical of a rock with microcracks and equant pores (Walsh 1965; Karner *et al.* 2003, 2005), in agreement with microstructural observations of the intact rock (Fig. 1). From mechanical data (Fig. 3a), the non-linearity at the beginning of the loading shows crack closure (Walsh 1965), up to a hydrostatic stress of 52 MPa. All cracks are considered to be closed at isostatic stress above 52 MPa. Porosity due to microcracks is estimated to be around $\phi_c = 0.07$ per cent. Crack closure pressure and crack porosity are similar to that obtained by Vajdova *et al.* (2004) on their samples of Tavel limestone (40 MPa and 0.1 per cent, respectively).

Measured static ($K_{stat} = 26.7$ GPa for $P_c \geq 52$ MPa) and dynamic ($K_{dyn} = 26.9$ GPa for $P_c \geq 52$ MPa) moduli are very close for white Tavel limestone, in contrast with what is commonly observed (Eissa & Kazi 1988; Fiona & Cook 1995; Ciccotti & Mulargia 2004). This could be explained by the microstructure of Tavel limestone, which

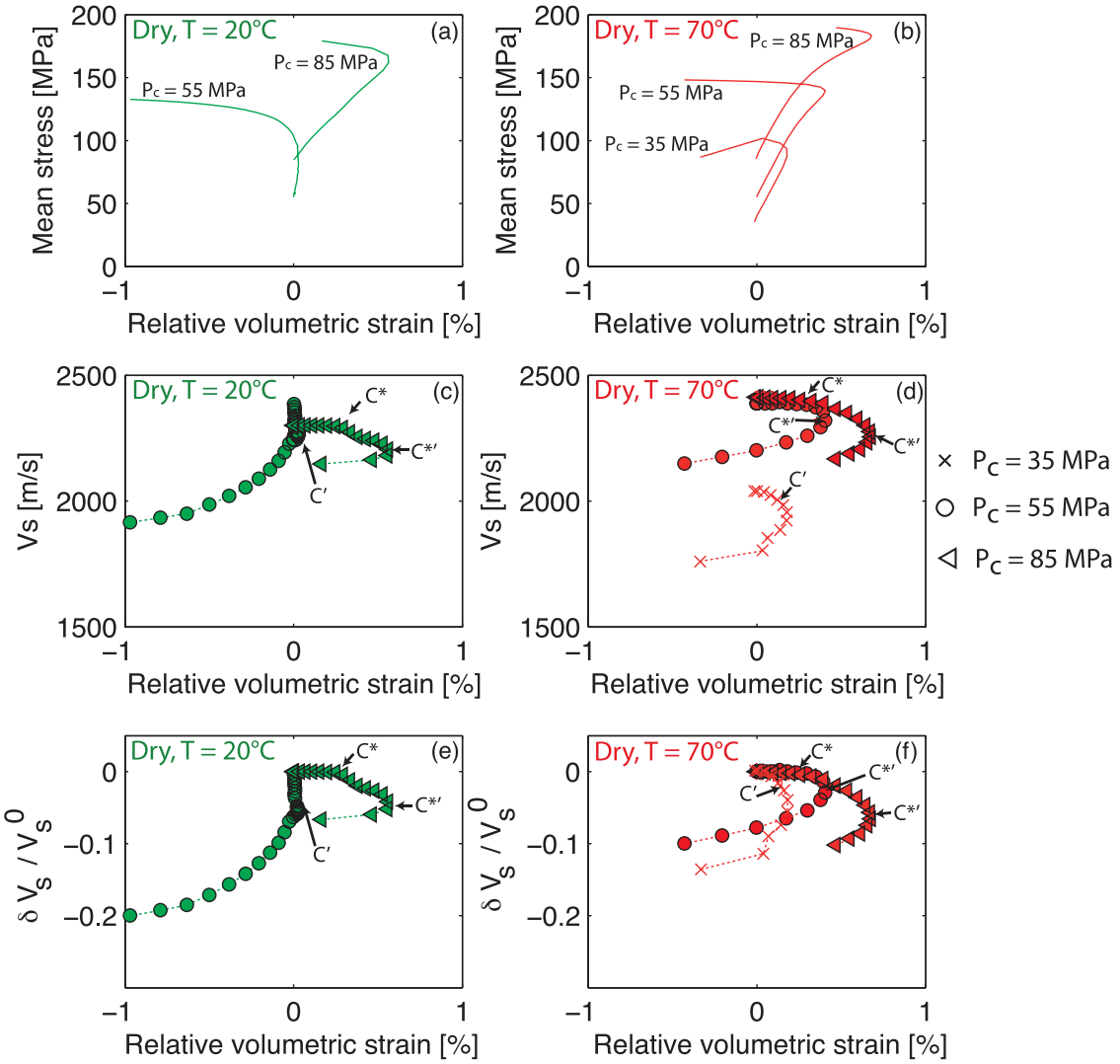

Figure 9. Compilation of mechanical and *S*-waves data for selected experiments (same as those presented in Fig. 8). Relative volumetric strain versus mean stress is shown for reference in (a) and (b) for dry experiments at 20 °C and dry experiments at 70 °C, respectively. Note that strains are 'relative strains', that is, the zero strain is that at the end of the hydrostatic loading. (c) and (d) show the evolution of *S*-wave velocities perpendicular to σ_1 versus the relative volumetric strain for the two sets of experiments. (e) and (f) show the evolution of $\delta V_s / V_s^0$ versus relative volumetric strain, where V_s^0 is the *S*-wave velocity at the beginning of the triaxial loading.

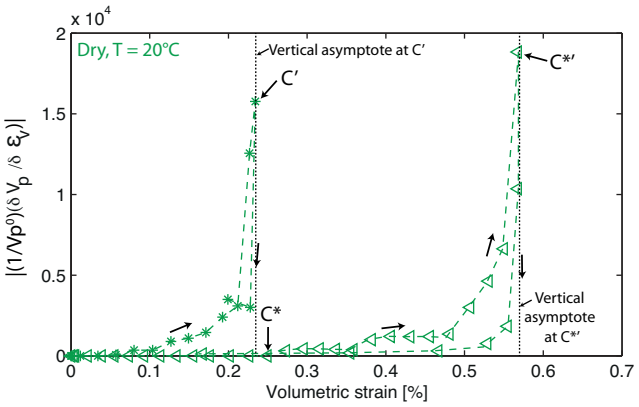

Figure 10. The absolute value of the *P*-wave velocity derivative with respect to the volumetric strain is plotted versus the volumetric strain for experiments conducted at $P_c = 20$ and 85 MPa in dry conditions. The maximum value is found for C' and $C^{*\prime}$ for the brittle and semi-brittle behaviours, respectively.

is composed of cemented micritic grains (Fig. 1). All cracks are closed at $P_c \geq 52$ MPa and grain boundaries are well cemented (Fig. 1b), thus reducing the difference between static and dynamic moduli because grain sliding and rearrangements are prevented (Regnet *et al.* 2015b).

To interpret theoretically and quantitatively the evolution of the ultrasonic velocities, we consider a porous rock as made of a mixture of solid grains, spherical pores, and penny-shaped cracks. Inverted crack densities offer a quantitative description of the damage due to cracks (Nasseri *et al.* 2007; Mallet *et al.* 2013, 2014). More precisely, Mallet *et al.* (2013, 2014) showed that crack densities inverted from ultrasonic velocities in a cracked glass are in very good agreement with optically measured ones. Here, the concept of crack density is understood as a statistical generalization of the concept of porosity for non-spherical inclusions. For example, an elongated porous space between two grains is considered as a crack (Guéguen & Kachanov 2011; Ghabezloo 2015). Using Kachanov (1993), the effective elastic properties of the porous rock may be

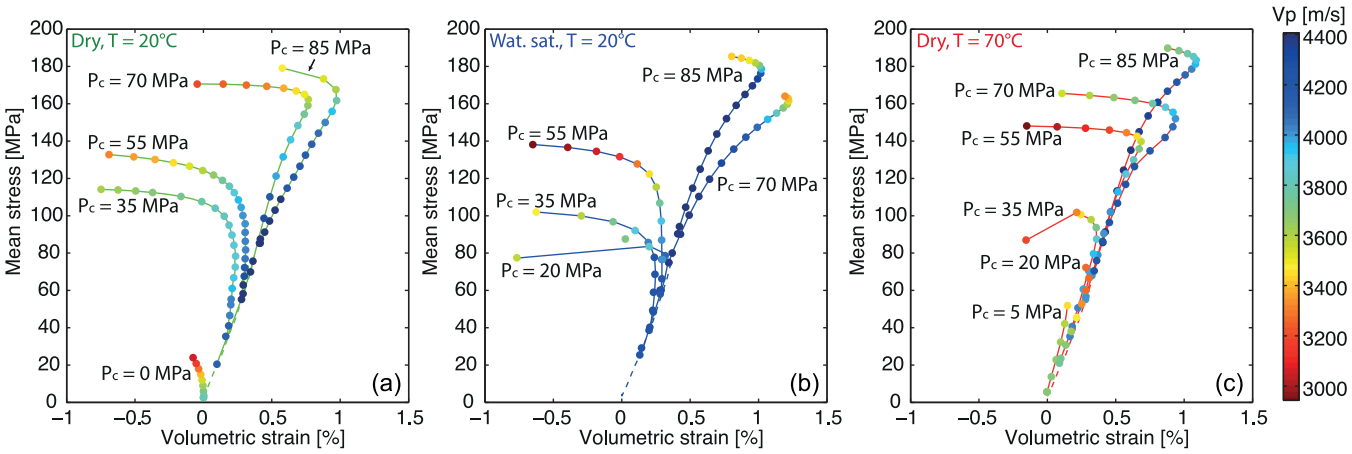

Figure 11. Representative data for *P*-wave velocity evolution during deformation. Volumetric strain is plotted versus the mean stress *P*. The confining pressure is indicated on each curve. The colour of the dots represents *P*-wave velocity perpendicular to σ_1. The colour caption is given on the right.

expressed in a unique manner as a function of the overall porosity ϕ and the crack density ρ_c. The crack density is defined as:

$$\rho_c = \frac{1}{V}\sum_{i=1}^{n} c_i^3, \tag{3}$$

where c_i is the radius of the ith crack and N is the total number of cracks embedded in the representative elementary volume (REV) V. Note that, from eq. (3), the dominant factor in the crack density is not the number of cracks per unit volume, but the crack length c.

In dry conditions, the effective dynamic bulk modulus K (which can be directly inverted from a combination of the *P*- and *S*-wave velocities) can be expressed as (Kachanov 1993; Fortin *et al.* 2007):

$$\frac{K_0}{K} = 1 + \frac{\rho_c}{1-\phi}\frac{h}{1-2\nu_0}\left(1 - \frac{\nu_0}{2}\right), \tag{4}$$

where K_0 is the bulk moduli of the crack-free matrix, ν_0 is Poisson's ratio of the crack-free matrix, ρ_c is the crack density and h is a factor given (for a penny-shaped geometry) by

$$h = \frac{16\left(1-\nu_0^2\right)}{9(1-\nu_0/2)}. \tag{5}$$

The elastic properties K_0 and ν_0 of the calcite aggregate composed of the solid matrix and embedded pores were estimated from velocities measured at $P_c = 85$ MPa, a pressure far above the crack closing pressure (see Section 3.1 and Fig. 3).

As pressure is increased isostatically from 0 to 52 MPa, the isotropic crack density decreased from 0.035 to 0 (Fig. 3c). Above 52 MPa, crack density remains constant at a value of 0 (Fig. 3c), due to the fact that *P*- and *S*-wave velocities remain constant (Fig. 3b). Inverted crack density evolution is consistent with the crack closure inferred from mechanical data (Fig. 3a).

Following Walsh (1965), the crack closure pressure $P_{\rm cl}$ for isotropic stress state can be related to the crack aspect ratio defined as $\xi = w/2c$, where w is the crack aperture:

$$P_{\rm cl} = \frac{\pi \xi E_0}{4\left(1-\nu_0^2\right)}. \tag{6}$$

Using the elastic properties of the crack-free material and $P_{cl} = 52$ MPa, eq. (6) gives $\xi = 1.9 \times 10^{-3}$, a value close to those reported in the literature (Baud *et al.* 2000a). If cracks are assumed to be characterized by a penny-shape geometry, then crack porosity is given by (Guéguen & Kachanov 2011):

$$\phi^{\rm crack} = 2\pi\rho_c\langle\xi\rangle, \tag{7}$$

where $\langle\xi\rangle$ is the average crack aspect ratio defined as $\langle\xi\rangle = \langle w/2c\rangle$. Taking $\langle\xi\rangle = 1.9 \times 10^{-3}$ and $\rho = 3.5 \times 10^{-2}$ (isotropic crack density inverted at $P_c = 0$ MPa), one finds an initial crack porosity $\phi_c^i \simeq 0.042$ per cent. This value is of the order of the crack volume inferred from the mechanical data shown in Fig. 3(a) ($\phi_c = 0.07$ per cent).

Above the crack closure pressure, the rock is assumed to be composed of the solid matrix and embedded pores. Walsh (1965) modelled the effective bulk modulus K of dilute spherical pores embedded in an elastic matrix as:

$$\frac{K_m}{K} = 1 + \frac{3}{2}\frac{(1-\nu_m)}{(1-2\nu_m)}\frac{\phi}{(1-\phi)}, \tag{8}$$

where ϕ is the porosity of the equant pores, and K_m and ν_m are the intrinsic incompressibility and Poisson ratio of the solid grain, respectively. For a calcite aggregate at 300 MPa pressure, the Reuss averages are $K_m = 73$ GPa for the intrinsic bulk modulus and $\nu_m = 0.33$ for the intrinsic Poisson's ratio (Simmons & Wang 1971). Using these values, the bulk modulus found for our 14.7 per cent porosity limestone is $K = 47.6$ GPa, which is larger than $K = 26.7$ GPa measured experimentally with static measurements. This discrepancy between theory and experimental data for limestones of porosity higher than 10 per cent was already observed by Vajdova *et al.* (2004), who explained it by the fact that the model considered dilute pores whereas interaction among the pores is likely to occur for high porosities. Another explanation could be that Walsh's (1965) model considers spherical pores embedded in a solid matrix. Considering a four-sided hypotrochoidal and a triangular pore, Zimmerman (1990) showed that the compressibility is twice and 1.6 times larger than that of a spherical pore of same volume, respectively. As shown by Fig. 1 (a), pores in Tavel limestone are not spherical, which could explain the discrepancy between experimental and theoretical values.

4.2 Crack densities under triaxial stresses

According to previous works (e.g. Winkler & Murphy 1995; Guéguen & Kachanov 2011), elastic solutions can be used to interpret ultrasonic wave velocities. Under triaxial stresses, our results show that ultrasonic wave velocities depend on the pathway, indicating that cracks are not randomly oriented. The maximum decrease is observed for the pathway perpendicular to σ_1 (90°), which suggests that the propagating and/or nucleating cracks are

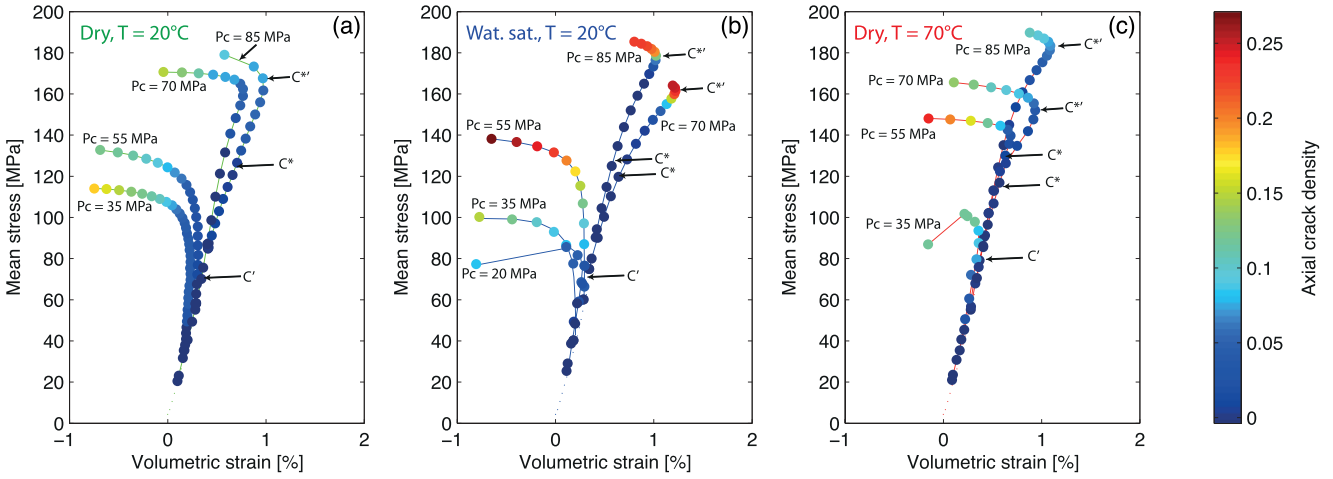

Figure 12. Volumetric strain plotted versus mean stress for experiments performed under dry conditions at 20 °C (a), water-saturated conditions at 20 °C (b) and dry conditions at 70 °C (c). Axial crack density evolution is superimposed for each experiment. The colour caption is given on the right.

mainly axial (Ayling *et al.* 1995; Mavko *et al.* 1995; Fortin *et al.* 2011). Thus, we invert ultrasonic wave velocities in terms of axial crack density (Sayers & Kachanov 1995) assuming: (1) a transverse isotropic crack geometry; (2) an isotropic matrix, in agreement with the isotropic ultrasonic waves velocities measured under hydrostatic conditions; (3) non-interacting cracks, an assumption which is valid for crack densities up to at least 0.15 and probably 0.2–0.25 (Grechka & Kachanov 2006); (4) a random crack centre distribution; and (5) penny-shape cracks of radius c and aperture w. The effective mechanical properties of the calcite aggregate composed of the solid matrix and embedded pores (Young modulus $E_0 = 32.8$ GPa and Poisson's ratio $\nu_0 = 0.29$) were estimated from velocities measured at $P_c = 85$ MPa, a pressure far above the crack closing pressure (see Fig. 3). The detailed procedure is given in Appendix A.

When the differential stress is increased, the evolution of the crack density depends upon the deformation mode. The axial crack density remains constant during the elastic compaction of all experiments (Fig. 12). Beyond that stage, changes in crack density depend upon the confining pressure. In the brittle regime, the axial crack density increases immediately beyond the onset of dilatancy (C') and reaches values between 0.1 and 0.27 at macroscopic failure (Fig. 12). Inverted crack densities are slightly higher in water-saturated conditions than in dry ones, suggesting that water enhances crack propagation. At $T = 70$ °C, crack densities are almost identical to those measured in dry conditions at $T = 20$ °C.

In the semi-brittle regime, axial crack density increases beyond the onset of inelastic compaction (C^*). However, between C^* and the post-yield onset of dilatancy ($C^{*\prime}$), the induced crack density remains low. For example, in dry conditions, for $P_c = 70$ MPa and $T = 70$ °C, the crack density increases from 0 at C^* to 0.01 at $C^{*\prime}$. During the inelastic compaction stage and as the post-yield onset of dilatancy ($C^{*\prime}$) is approached, crack density increase rate with respect to the volumetric strain accelerates. Beyond $C^{*\prime}$, crack density increases rapidly up to 0.15–0.25 (Fig. 12). In water-saturated conditions, crack densities are slightly higher than in the dry case, especially for the experiments performed at $P_c = 70$ MPa. At $T = 70$ °C, crack densities are slightly lower than at $T = 20$ °C, suggesting that temperature enhances plastic phenomena.

4.3 Onset and development of dilatancy in the brittle regime

Brittle faulting can be modelled by a sliding wing crack model (Cotterell & Rice 1980). With this interpretation, the end of the elastic behaviour in the brittle regime (onset of dilatancy denoted C') is considered as the point of initiation of wing cracks. Assuming an isotropic rock (in agreement with path-independent ultrasonic wave velocities under hydrostatic pressure), initial cracks are considered as randomly oriented. Under triaxial stresses, wing cracks should preferentially initiate at an angle of $\psi = (1/2)\tan^{-1}(1/\mu)$ to the largest remote compressive stress σ_1, where μ is the friction coefficient of the initial crack. The onset of dilatancy is expected at an axial stress (Cotterell & Rice 1980; Horii & Nemat-Nasser 1986; Ashby & Sammis 1990):

$$\sigma_1 = \frac{\sqrt{1+\mu^2}+\mu}{\sqrt{1+\mu^2}-\mu}\sigma_3 + \left(\frac{\sqrt{3}}{\sqrt{1+\mu^2}-\mu}\right)\frac{K_{IC}}{\sqrt{\pi a}}, \quad (9)$$

where a is the radius of initial cracks and K_{IC} is the intrinsic fracture toughness of the material. From linear regressions of the data (Fig. 13), one gets $\mu = 0.6 \pm 0.1$ and $K_{IC}/(\pi a)^{1/2} = 17.1 \pm 1$ MPa for the experiments performed in dry conditions at $T = 20$ °C and $T = 70$ °C (Table 3).

For water saturated experiments, linear regressions lead to $\mu = 0.35 \pm 0.1$. This reduction of friction coefficient in water-saturated conditions was already observed for sandstones (Baud *et al.* 2000b) but the friction coefficient drop was only 10 per cent. For water saturated experiments, one gets from the data $K_{IC}/(\pi a)^{1/2} = 16 \pm 1$ MPa, a value that is slightly lower than that in dry conditions ($K_{IC}/(\pi a)^{1/2} = 17.1 \pm 1$ MPa). The decrease of surface energy can be calculated considering that the crack initial mean size, a, is the same for dry and water saturated experiments:

$$\frac{K_{IC}^{dry}}{K_{IC}^{wat.}} = \left(\frac{\gamma^{dry}}{\gamma^{wat.}}\right)^{1/2} = 1.07 \pm 0.06, \quad (10)$$

where γ^{dry} and $\gamma^{wat.}$ are the dry and water-saturated surface energies, respectively. The ratio between dry and water saturated surface energies is then: $\gamma^{dry}/\gamma^{wat.} = 1.14 \pm 0.12$. The ratio between dry and water saturated surface energies obtained in this study is of the same order as what de Leeuw & Parker (1997) obtained by numeric

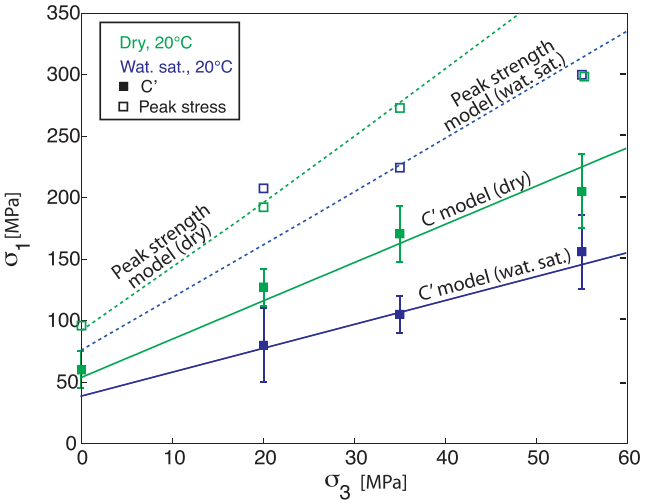

Figure 13. Experimental stress states C' and peak stresses (in green for experiments performed in dry conditions and in blue for experiments performed in water-saturated conditions) are compared to theoretical predictions. Predicted stresses at C' and peak stresses are modelled by eqs (9) and (11), respectively. Model C' and peak stresses are represented by the plain and dashed lines, respectively.

Table 3. Wing crack and energy parameters inferred from mechanical data.

Condition	μ	$K_{IC}/(\pi a)$ (MPa)	D_0
Dry	$\mu = 0.6 \pm 0.1$	17.1 ± 1	0.055
Wat. sat.	$\mu = 0.35 \pm 0.1$	16 ± 1	0.055

simulations for calcite. This ratio is also comparable to that obtained by Baud *et al.* (2000b) on sandstones, which can be explained by the fact that quartz and calcite have similar surface energies (Friedman *et al.* 1972). Water adsorption on the internal pore surface leads to a reduction of surface free energy (de Leeuw & Parker 1997; Røyne *et al.* 2011, 2015) that chemically weakens the rock (Rutter 1972; Henry *et al.* 1977; Baud *et al.* 2000b). This observation of chemical weakening of the rock is in agreement with the higher crack density obtained during triaxial deformation in water-saturated conditions than in dry conditions (Figs 12a and b).

An increase of 50 °C in temperature does not modify the differential stress at the onset of dilatancy (C') and the development of dilatancy. Qualitatively similar mechanical behaviour and similar strains are observed at $T = 20$ °C and $T = 70$ °C (Figs 4d and f).

4.4 Failure envelope in the brittle regime

Previously published 2-D (plane strain) models (Ashby & Sammis 1990) are used to analyse failure. To a first approximation (detailed explanation is given in Appendix B), the failure envelope for the wing crack model (Horii & Nemat-Nasser 1986; Ashby & Sammis 1990; Kemeny & Cook 1991; Baud *et al.* 2000a) can be described by a linear relation:

$$\sigma_1 = A(\mu, D_0)\sigma_3 + B(\mu, D_0)\frac{K_{IC}}{\sqrt{\pi a}}, \quad (11)$$

where A and B are constants which depend on the friction coefficient μ and $D_0 = \pi(a\cos\psi)^2 N_A$, where N_A is the number of sliding cracks of uniform orientation ψ per unit area initially present. The constant D_0 characterises the initial damage. Using eq. (11) with $K_{IC}/(\pi a)^{1/2}$ and μ that were inverted from eq. (9) for dry conditions, one finds $D_0 = 0.055$, a lower value than that reported in Vajdova *et al.* (2004) for white Tavel (0.28). As shown by Fig. 13, experimental data are in reasonable agreement with the obtained theoretical prediction (green dashed line). A question remains: Is $D_0 = 0.055$ in agreement with the initial crack density inverted from ultrasonic wave velocities? From velocity data, inverted initial 3-D isotropic crack density is $\rho = 0.035$. The failure envelope for the wing crack model (eq. 11) is 2-D. Converting 3-D crack density into 2-D leads to $\rho_{2D} = \rho_{3D}^{2/3}$. Then, from ultrasonic wave velocity measurements and using $\psi = (1/2)\tan^{-1}(1/\mu)$, one gets $D_0 = \pi\rho^{2/3}\cos^2\psi = 0.25$. The value inverted from the failure envelope (eq. 11) being $D_0 = 0.055$, this suggests that the sliding cracks (those of uniform orientation around ψ) represent approximately 20 per cent of the initially present cracks.

Model predictions for peak strength depend upon μ, K_{IC}, D_0 and a. The initial damage D_0 and initial crack length a are likely to remain constant whatever the pore fluid is but μ and K_{IC} are modified in the presence of water compared to dry conditions. Using $K_{IC}/(\pi a)^{1/2} = 16$ MPa, $\mu = 0.35$ (values inverted from C' model for water-saturated conditions) and $D_0 = 0.055$ (same value as for dry samples), model predictions for peak strengths are lower in water-saturated conditions than in dry ones (Fig. 13). A water-weakening effect is experimentally evidenced for the onset of dilatancy (C') but not for the peak strength, which is similar to what was observed in cracked granites (Wang *et al.* 2013) but not to what has been observed in sandstones (Baud *et al.* 2000b). Why is the onset of dilatancy affected by the presence of water but not the peak strength? Samples are fully saturated, and the characteristic time for diffusion is in the order of 1 s, which is a very short time compared to that of our experiments (between 10 min and 1 hr). However, during the dynamic fracture propagation, it is possible that the full saturation is not maintained, and that the fracture tip remains dry.

4.5 From inelastic compaction to dilatancy in the semi-brittle regime

For $P_c \geq 70$ MPa at $T = 20$ °C and $P_c \geq 55$ MPa at $T = 70$ °C, inelastic compaction of Tavel limestone is observed beyond the stress state C^*. Beyond elastic compaction, Dautriat *et al.* (2011b) showed that cataclastic compaction is coupled with an ultrasonic wave velocity decrease by approximately 30 per cent in a very porous limestone (Estaillades limestone, porosity: 28 per cent). This observation also holds for porous sandstones (Fortin *et al.* 2005, 2007). In our experiments, V_p and V_s decrease by 10 per cent to 15 per cent between C^* and $C^{*\prime}$ (Figs 8 and 9), and inverted crack densities remain low between these stress states (Figs 12 and 14). The ultrasonic wave velocities decrease rate with respect to volumetric strain increases as the post-yield onset of dilatancy ($C^{*\prime}$) is approached (Fig. 10), indicating that cracks develop although macroscopic inelastic compaction is recorded. At this stage, compaction due to plastic pore collapse and dilatancy due to development of cracks take place simultaneously. However, compaction strain associated with pore collapse appears to be predominant. Microstructural analyses show an intense twinning activity (Fig. 7f), and small cracks that did not coalesce in large sparites (Fig. 7g and h). These observations suggest that deformation beyond C^* in the semi-brittle regime and inelastic pore collapse are controlled by plastic micromechanisms associated with some microcracking. This conclusion is in good agreement with results from Vajdova *et al.* (2004) who showed that limestones with low porosities ($\leq$15 per cent) undergo inelastic compaction associated with dislocation slip processes, twinning and some microcracking. Baud *et al.* (2000a) drew similar conclusions and interpreted shear-enhanced compaction in Solnhofen limestone

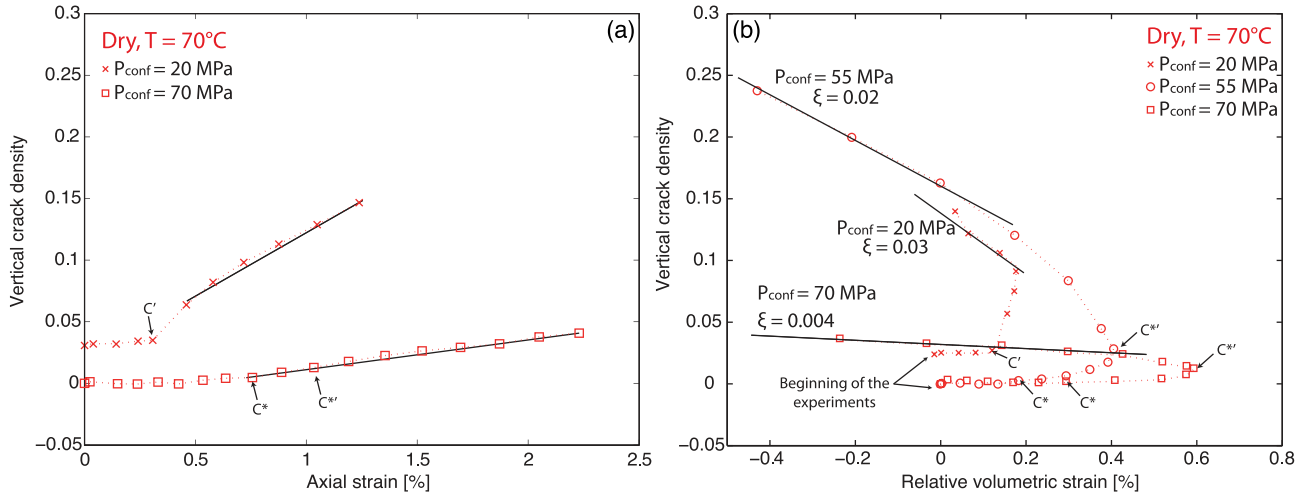

Figure 14. (a) Evolution of axial crack density as a function of axial strain. The rate of increase is linear with respect to axial strain and increases with the increase of the confining pressure. (b) Cracks density is plotted as a function of volumetric strain. The slope of the linear fit corresponds to the mean crack aspect ratio $\langle \xi \rangle$ (eq. 14).

as resulting from plastic collapse of spherical pores embedded in a solid matrix, as initially modelled by Curran & Carroll (1979). The sensitivity of the onset of inelastic compaction (C^*) to the variations of the experimental conditions (pore fluid and temperature) explored by our experiments seems to be blurred. Possibly the range in investigated temperatures is simply too small.

At the post-yield onset of dilatancy ($C^{*\prime}$), the competition between shear-enhanced compaction and dilatancy leads to a switch from overall compaction to overall dilatancy. Around $C^{*\prime}$, the decrease of V_p and V_s compared to the volumetric change is maximum (Fig. 10, experiment performed at $P_c = 85$ MPa). Volumetric strain close to peak stress can be due to crack propagation but also to shearing and rotation of fragments (Peng & Johnson 1972; Guéguen & Boutéca 2004; Vajdova *et al.* 2012). Thus, the decrease of ultrasonic wave velocities is due to crack nucleation and/or propagation but may also be affected by the porosity induced by rotation of fragments.

Water saturation and a temperature increase of $\Delta T = 50\,^{\circ}$C have no measurable effect on the post-yield onset of dilatancy ($C^{*\prime}$). Water saturation might promote the development of cracks beyond the onset of inelastic compaction (C^*) but not sufficiently to observe a change in the macroscopic behaviour and on the post-yield onset of dilatancy ($C^{*\prime}$). As no temperature effect is observed on $C^{*\prime}$ (Fig. 5), it may be again that a temperature increase of $\Delta T = 50\,^{\circ}$C is not sufficient to get a measurable effect on $C^{*\prime}$.

The inelastic compaction observed in this study is qualitatively similar to that of Solnhofen limestone (Baud *et al.* 2000a) and of Tavel and Indiana limestones (Vajdova *et al.* 2004, 2010). A comparison of the yield envelope obtained by Vajdova *et al.* (2004) for a 10.5 per cent porosity Tavel limestone with those reported in this paper for a porosity of 14.7 per cent (Fig. 15) underlines that porosity plays a major role in lowering the confining pressure at which the brittle-ductile transition occurs, in agreement with the work of Wong *et al.* (1997).

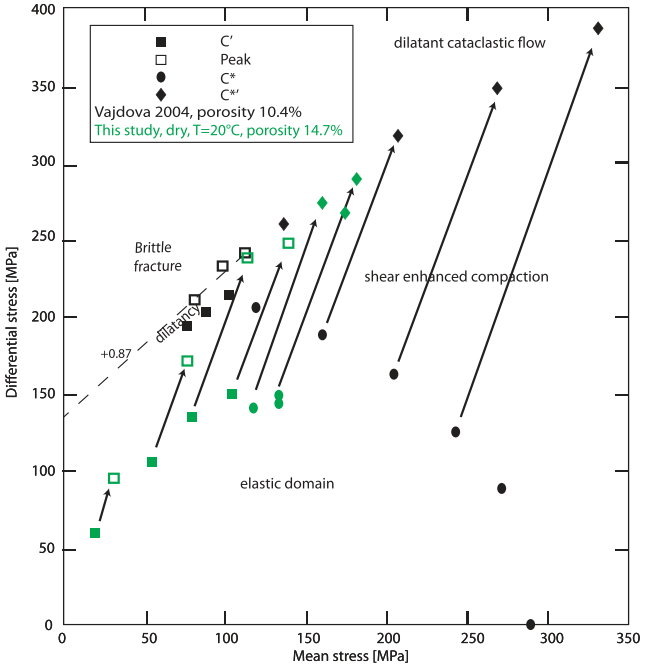

Figure 15. The failure envelope (dry conditions at 20 °C) from this study is compared with the one obtained by Vajdova *et al.* (2004).

4.6 Crack geometry

Beyond the onset of dilatancy (C') and the post-yield onset of dilatancy ($C^{*\prime}$), ultrasonic wave velocities revealed important variations (Figs 8 and 9), which may be interpreted as variations in crack densities. Beyond these stress states, crack density increases almost linearly with axial strain (Fig. 14a). The linearity observed in this study is consistent with previous observations made by Brantut *et al.* (2011) on gypsum deformed across the brittle-ductile transition.

As the concept of crack density is understood as a statistical generalization of the concept of porosity for non-spherical inclusions, the volumetric strain due to shearing and rotation of grains and porosity that they induce is taken into account in the crack porosity. Considering crack densities inverted from ultrasonic wave velocities in addition to mechanical data makes it possible to derive a mean aspect ratio parameter for propagating cracks. Focusing on volumetric strain, in a first approximation, inelastic volumetric strain, ε^{in}, can be decomposed as

$$\varepsilon^{\text{in}} \approx \Delta\phi = \Delta\phi^{\text{cracks}} + \Delta\phi^{\text{pore}}, \tag{12}$$

where $\Delta\phi$ is the porosity variation, $\Delta\phi^{\text{cracks}}$ is the porosity variation due to cracks and $\Delta\phi^{\text{pore}}$ is the porosity variation due to pore collapse. Note that during crack propagation and pore collapse, $\Delta\phi^{\text{cracks}}$ and $\Delta\phi^{\text{pore}}$ are of opposite sign. In the brittle regime, dilatancy is occurring beyond C' and thus $|\Delta\phi^{\text{cracks}}| > |\Delta\phi^{\text{pore}}|$. In the semi-brittle regime, $|\Delta\phi^{\text{cracks}}| < |\Delta\phi^{\text{pore}}|$ between the onset of inelastic compaction (C^*) and the post-yield onset of dilatancy ($C^{*\prime}$) and beyond $C^{*\prime}$, $|\Delta\phi^{\text{cracks}}| > |\Delta\phi^{\text{pore}}|$. Therefore, beyond the onset of dilatancy (C') in the brittle regime and beyond the post-yield onset of dilatancy ($C^{*\prime}$) in the semi-brittle regime, one gets:

$$\Delta\phi^{\text{cracks}} = \varepsilon^{\text{in}}. \tag{13}$$

Combining eqs (13) and (7), one gets:

$$\frac{\partial\varepsilon^{\text{in}}}{\partial\rho_c} = 2\pi\langle\xi\rangle. \tag{14}$$

Fig. 14(b) gives the relative volumetric strain (i.e. relative to the end of the hydrostatic loading) versus the inverted crack density for three experiments performed at 20 MPa, 55 MPa and 70 MPa, and $T = 70\,^{\circ}$C.

In the brittle regime, that is, for $P_c = 20$ MPa, the initial axial crack density is 0.02 and remains constant until the onset of dilatancy (C') is reached. Then, crack density increases at almost constant relative volumetric strain. The lack of volume change may be explained by a balance between dilatation associated with cracking and elastic compaction. Finally, a linear trend appears between the axial crack density and the relative volumetric strain. Note that this appears when the crack density has increased by a factor of 5. Using eq. (14), the average crack aspect ratio can be estimated to be $\langle\xi\rangle = 0.03$.

In the semi-brittle regime, that is, for $P_c = 55$ and 70 MPa, the initial crack density is 0, as the confining pressure is higher than the pre-existing crack closure pressure. Crack density remains at 0 below the onset of inelastic compaction (C^*). Between C^* and the post-yield onset of dilatancy ($C^{*\prime}$), crack density increases to 0.025 and 0.01 for experiments performed at $P_c = 55$ MPa and $P_c = 70$ MPa, respectively. During this stage, inelastic compaction is taking place as evidenced by volumetric strain evolution but as ultrasonic wave velocities are not strongly sensitive to spherical pores (Fortin *et al.* 2007), they cannot provide a useful information on variations of equant porosity. At some point beyond the post-yield onset of dilatancy ($C^{*\prime}$), a linear trend between the axial crack density and the relative volumetric strain is observed, and the average crack aspect ratio is found to be equal to $\langle\xi\rangle = 0.02$ and $\langle\xi\rangle = 0.004$ for the experiments performed under a confining pressure of 55 MPa and 70 MPa, respectively. Beyond the onset of dilatancy (C') in the brittle regime or the post-yield onset of dilatancy ($C^{*\prime}$) in the semi-brittle regime, the linear trend between the axial crack density and the relative volumetric strain suggests that crack propagate at constant average crack aspect ratio.

The linear relations between crack densities and volumetric strains (Fig. 14b) give decreasing average crack aspect ratios of 0.03, 0.02 and 0.004 for confining pressures increasing from $P_c = 20$, 55 and to 70 MPa, respectively. Note that these values are all higher than aspect ratios calculated for pre-existing cracks (Section 4.1). This can be explained by the fact that (i) the vertical cracks induced by the deformation have a geometry different from that of pre-existing cracks and (ii) the inverted axial crack density during triaxial loading may take into account shearing and rotation of grains.

Using linear elastic fracture mechanics for non-interacting opening mode fractures under two-dimensional, plane strain conditions in an homogeneous isotropic medium, Pollard & Segall (1987) found:

$$\xi = \Delta\sigma_I \frac{2(1-\nu^2)}{E}, \tag{15}$$

where $\Delta\sigma_I$ is the opening mode driving stress, ν is Poisson's ratio and E is Young's modulus. Note that this equation is similar to eq. (6), except that stress is not isotropic here. Using the previously presented model for crack growth from initial flaws (Ashby & Sammis 1990), the opening driving stress is the wedging force F_w on the pre-existing crack of radius a, which depends on σ_1 and σ_3 as:

$$F_w = (A_1\sigma_1 - A_3\sigma_3)a, \tag{16}$$

where A_1 and A_3 are constants which depend on the friction on the pre-existing crack. Thus, linear fracture mechanics for non-interacting opening mode fractures predicts a constant aspect ratio for cracks propagating at constant stress state. During constant strain rate experiments, the confining pressure is constant but the differential stress is not. However, for each experiment, constant aspect ratios are observed when the axial stress does not increase much (Fig. 4f). For example, focusing on the experiment performed at a confining pressure of 70 MPa, crack propagation at constant aspect ratio is observed when crack propagation is occurring at constant confining pressure and when axial stress variations remain lower than 10 MPa.

The aspect ratio is linearly correlated to the opening mode driving stress (eq. 15), which in turn depends on the axial stress and the confining pressure. The axial stress tends to increase the aspect ratio whereas the confining pressure tends to decrease it. In our experiments, the aspect ratio decreases as the axial stress and confining pressure increase. This means that in the stress conditions of our study, the aspect ratio is controlled by the confining pressure rather than by the axial stress. This observation (1) is in agreement with Lehner & Kachanov (1996), who showed that the confining pressure has a major influence on crack growth from pre-existing flaws, and (2) can be explained by the fact that in eq. (16), according to Ashby & Sammis (1990):

$$A_3 = A_1\left(\frac{(1+\mu^2)^{1/2}+\mu}{(1+\mu^2)^{1/2}-\mu}\right), \tag{17}$$

where μ is the friction coefficient on the pre-existing crack. Finally, using $\mu = 0.6$ as found in this study, one gets $A_3 \sim 3.12\,A_1$. This simple approach could be improved by a more detailed model (Renshaw & Park 1997; Olson 2003).

5 CONCLUDING SUMMARY

In this study, we show the complexity of the mechanisms accommodating the deformation of a porous limestone at different confining pressures and explore the role of pore fluid and temperature. At low confining pressure, inelastic deformation is due to the development of cracks, which leads to the macroscopic failure of the sample. At high confining pressure, the onset of inelastic compaction is associated with shear-enhanced compaction. Then, beyond a stress state denoted $C^{*\prime}$, the macroscopic volumetric strain switches to dilatancy that eventually leads to localized failure. The measurements of ultrasonic wave velocities during the experiments suggest the ongoing interplay of shear-enhanced compaction and development of cracks between the onset of inelastic compaction C^* and post-yield onset of dilatancy $C^{*\prime}$. The post-yield onset of dilatancy ($C^{*\prime}$) marks a change in relative dominance rather than in occurring mechanisms.

The comparison of our data to that reported in Vajdova *et al.* (2004) on the same rock but with a smaller average porosity of 10.5 per cent (Fig. 15) indicates that porosity plays a major role in reducing the confining pressure at which the brittle ductile transition occurs, in agreement with the work of Wong *et al.* (1997).

We inverted ultrasonic wave velocities to axial crack density. Above the onset of dilatancy C' (brittle regime) or post-yield onset of dilatancy $C^{*'}$ (semi-brittle regime), the linear trend between the axial crack density and the relative volumetric strain suggest that cracks propagate at constant average crack aspect ratio. The calculated average crack aspect ratio decreases as the confining pressure increases.

Water has a weakening effect on the onset of dilatancy in the brittle regime but no effect could be identified on the peak strength, on stress state at the onset of inelastic compaction (C^*), nor on the stress state at the post-yield onset of dilatancy ($C^{*'}$). An increase in temperature of $\Delta T = 50\,^{\circ}\mathrm{C}$ (from 20 °C to 70 °C) has no effect on the onset of dilatancy in the brittle regime nor on the peak strength at confining pressures leading to brittle behaviour. While the increase of temperature lowers the confining pressure at which the brittle-ductile transition occurs, it does not lead to changes in the values of the stress states at the onset of inelastic compaction (C^*) and post-yield onset of dilatancy ($C^{*'}$).

ACKNOWLEDGEMENTS

The first author thanks Patrick Baud and Serge Lugan for providing the block of Tavel limestone. The authors are grateful to Simon Hallais, Alexandre Tanguy, Damien Deldicque and Yves Pinquier for technical support. AN is also grateful to Philippe Marchina, Teng-Fong Wong, Christian David, Alexandre Schubnel, Harsha S. Bhat, Patrick Baud, Yves M. Leroy and Philippe Robion for stimulating discussions. The authors also thank J. Renner, G. Dresen and an anonymous reviewer, who provided helpful constructive reviews that greatly improved the manuscript. This project was funded by a grant provided by Total No FR00006158.

REFERENCES

Ashby, M. & Sammis, C.G., 1990. The damage mechanics of brittle solids in compression, *Pure appl. Geophys.,* **133,** 489–521.

Atkinson, B.K. & Meredith, P., 1987. The theory of subcritical crack growth with applications to minerals and rocks, in *Fracture Mechanics of Rock,* pp. 111–166, ed. Atkinson, B.K., Academic Press.

Ayling, M.R., Meredith, P.G. & Murrell, S.A., 1995. Microcracking during triaxial deformation of porous rocks monitored by changes in rock physical properties, I. Elastic-wave propagation measurements on dry rocks, *Tectonophysics,* **245**(3), 205–221.

Baud, P., Schubnel, A. & Wong, T.-F., 2000a. Dilatancy, compaction, and failure mode in Solnhofen limestone, *J. geophys. Res.,* **105**(B8), 19 289–19 303.

Baud, P., Zhu, W. & Wong, T.-F., 2000b. Failure mode and weakening effect of water on sandstone, *J. geophys. Res.,* **105**(B7), 16 371–16 389.

Baud, P., Vinciguerra, S., David, C., Cavallo, A., Walker, E. & Reuschlé, T., 2009. Compaction and failure in high porosity carbonates: mechanical data and microstructural observations, *Pure appl. Geophys.,* **166,** 869–898.

Bemer, E. & Lombard, J., 2010. From injectivity to integrity studies of CO_2 geological storage chemical alteration effects on carbonates petrophysical and geomechanical properties, *Oil Gas Sci. Technol.,* **65,** 445–459.

Benson, P., Schubnel, A., Vinciguerra, S., Trovato, C., Meredith, P. & Young, R.P., 2006. Modeling the permeability evolution of microcracked rocks from elastic wave velocity inversion at elevated isostatic pressure, *J. geophys. Res.,* **111**(B4), doi:10.1029/2005JB003710.

Boutéca, M., Sarda, J. & Schneider, F., 1996. Subsidence induced by the production of fluids, *Rev. Inst. Fr. Pet.,* **51,** 349–379.

Brace, W., 1978. Volume changes during fracture and frictional sliding: a review, *Pure appl. Geophys.,* **116,** 603–614.

Brantut, N., Schubnel, A. & Guéguen, Y., 2011. Damage and rupture dynamics at the brittle-ductile transition: the case of gypsum, *J. geophys. Res.,* **116**(B1), doi:10.1029/2010JB007675.

Carslaw, H.S. & Jaeger, J.C., 1959. *Conduction of Heat in Solids,* 2nd edn, Clarendon Press.

Ciccotti, M. & Mulargia, F., 2004. Differences between static and dynamic elastic moduli of a typical seismogenic rock, *Geophys. J. Int.,* **157**(1), 474–477.

Clarke, D., Lawn, B. & Roach, D., 1986. *The Role of Surface Forces in Fracture,* Springer.

Costin, L., 1987. Time-dependent deformation and failure, in *Fracture Mechanics of Rock,* pp. 167–216, ed. Atkinson, B.K., Academic Press.

Cotterell, B. & Rice, J.R., 1980. Slightly curved or kinked cracks, *Int. J. Fract.,* **16,** 155–169.

Curran, J.H. & Carroll, M.M., 1979. Shear stress enhancement of void compaction, *J. geophys. Res.,* **84**(B3), 1105–1112.

Dautriat, J., Bornert, M., Gland, N., Dimanov, A. & Raphanel, J., 2011a. Localized deformation induced by heterogeneities in porous carbonate analysed by multi-scale digital image correlation, *Tectonophysics,* **503**(1), 100–116.

Dautriat, J., Gland, N., Dimanov, A. & Raphanel, J., 2011b. Hydromechanical behavior of heterogeneous carbonate rock under proportional triaxial loadings, *J. geophys. Res.,* **116**(B1), doi:10.1029/2009JB000830.

David, C., Wong, T.-F., Zhu, W. & Zhang, J., 1994. Laboratory measurement of compaction-induced permeability change in porous rocks: implications for the generation and maintenance of pore pressure excess in the crust, *Pure appl. Geophys.,* **143**(1), 425–456.

De Bresser, J. & Spiers, C., 1997. Strength characteristics of the r, f, and c slip systems in calcite, *Tectonophysics,* **272**(1), 1–23.

de Leeuw, N. & Parker, S., 1997. Atomistic simulation of the effect of molecular adsorption of water on the surface structure and energies of calcite surfaces, *J. Chem. Soc. Faraday Trans.,* **93**(3), 467–475.

Dresen, G. & Evans, B., 1993. Brittle and semibrittle deformation of synthetic marbles composed of two phases, *J. geophys. Res.,* **98**(B7), 11 921–11 933.

Duda, M. & Renner, J., 2013. The weakening effect of water on the brittle failure strength of sandstone, *Geophys. J. Int.,* **192**(3), 1091–1108.

Edmond, J. & Paterson, M., 1972. Volume changes during the deformation of rocks at high pressures, *Int. J. Rock Mech. Min. Sci. Geomech. Abstr.,* **9**(2), 161–182.

Eissa, E. & Kazi, A., 1988. Relation between static and dynamic Young's moduli of rocks, *Int. J. Rock Mech. Min. Sci. Geomech. Abstr.,* **25,** 479–482.

Evans, B., Fredrich, J.T. & Wong, T.-F., 1990. The brittle-ductile transition in rocks: recent experimental and theoretical progress, in *The Brittle-Ductile Transition in Rocks,* pp. 1–20, doi:10.1029/GM056p0001.

Fiona, T. & Cook, J., 1995. Effects of stress cycles on static and dynamic Young's moduli in Castlegate sandstone, in *Rock Mechanics: Proceedings of the 35th US Symposium*, p. 155.

Fortin, J., Schubnel, A. & Guéguen, Y., 2005. Elastic wave velocities and permeability evolution during compaction of Bleurswiller sandstone, *Int. J. Rock Mech. Min. Sci.,* **42**(7), 873–889.

Fortin, J., Guéguen, Y. & Schubnel, A., 2007. Effects of pore collapse and grain crushing on ultrasonic velocities and *Vp/Vs*, *J. geophys. Res.,* **112**(B8), doi:10.1029/2005JB004005.

Fortin, J., Stanchits, S., Vinciguerra, S. & Guéguen, Y., 2011. Influence of thermal and mechanical cracks on permeability and elastic wave velocities in a basalt from Mt. Etna volcano subjected to elevated pressure, *Tectonophysics,* **503**(1), 60–74.

Fredrich, J.T., Evans, B. & Wong, T.-F., 1989. Micromechanics of the brittle to plastic transition in Carrara marble, *J. geophys. Res.,* **94**(B4), 4129–4145.

Fredrich, J.T., Arguello, J.G., Deitrick, G.L. & de Rouffignac, E.P., 2000. Geomechanical modeling of reservoir compaction, surface subsidence, and casing damage at the Belridge diatomite field, *SPE Reservoir Eval. Eng.,* **3,** 348–359.

Friedman, M., Handin, J. & Alani, G., 1972. Fracture-surface energy of rocks, *Int. J. Rock Mech. Min. Sci.,* **9**(6), 757–764.

Ge, S. & Stover, S.C., 2000. Hydrodynamic response to strike-and dip-slip faulting in a half-space, *J. geophys. Res.,* **105**(B11), 25 513–25 524.

Ghabezloo, S., 2015. A micromechanical model for the effective compressibility of sandstones, *Eur. J. Mech. A,* **51,** 140–153.

Grechka, V. & Kachanov, M., 2006. Effective elasticity of fractured rocks: a snapshot of the work in progress, *Geophysics,* **71,** W45–W58.

Griggs, D.T., Turner, F.J. & Heard, H.C., 1960. Chapter 4: Deformation of rocks at 500° to 800 °C, in *Rock Deformation,* vol. 79, pp. 39–104, eds Griggs, D.T. & Handin, J., Geological Society of America Memoirs.

Guéguen, Y. & Boutéca, M., 1999. Mechanical properties of rocks: pore pressure and scale effects, *Oil Gas Sci. Technol.,* **54**(6), 703–714.

Guéguen, Y. & Boutéca, M., 2004. *Mechanics of Fluid-saturated Rocks,* Academic Press.

Guéguen, Y. & Kachanov, M., 2011. Effective elastic properties of cracked rocks—an overview, in *Mechanics of Crustal Rocks,* pp. 73–125, eds Leroy, Y.M. & Lehner, F.K., Springer.

Heap, M., Baud, P. & Meredith, P., 2009. Influence of temperature on brittle creep in sandstones, *Geophys. Res. Lett.,* **36**(19), doi: 10.1029/2009GL039373.

Heard, H.C., 1960. Chapter 7: Transition from brittle fracture to ductile flow in Solenhofen limestone as a function of temperature, confining pressure, and interstitial fluid pressure, in *Rock Deformation,* vol. 79, pp. 193–226, eds Griggs, D.T. & Handin, J., Geological Society of America Memoirs.

Henry, J.P., Paquet, J. & Tancrez, J., 1977. Experimental study of crack propagation in calcite rocks, *Int. J. Rock Mech. Min. Sci. Geomech. Abstr.,* **14**(2), 85–91.

Hexsel Grochau, M., Monteiro Benac, P., de Magalhaes Alvim, L., Sansonowski, R.C., da Motta Pires, P.R. & Villaudy, F., 2014. Brazilian carbonate reservoir: a successful seismic time-lapse monitoring study, *eading Edge,* **33**(2), 164–170.

Horii, H. & Nemat-Nasser, S., 1986. Brittle failure in compression-splitting, faulting and brittle-ductile transition, *Phil. Trans. R. Soc. A,* **319,** 337–374.

Hugman, R., III. & Friedman, M., 1979. Effects of texture and composition on mechanical behavior of experimentally deformed carbonate rocks, *AAPG Bull.,* **63**(9), 1478–1489.

Ji, Y., Hall, S.A., Baud, P. & Wong, T.-f., 2015. Characterization of pore structure and strain localization in majella limestone by x-ray computed tomography and digital image correlation, *Geophys. J. Int.,* **200**(2), 701–719.

Kachanov, M., 1993. *Elastic Solids with Many Cracks and Related Problems,* Academic Press.

Karner, S.L., Chester, F.M., Kronenberg, A.K. & Chester, J.S., 2003. Subcritical compaction and yielding of granular quartz sand, *Tectonophysics,* **377**(3), 357–381.

Karner, S.L., Chester, J.S., Chester, F.M., Kronenberg, A.K. & Hajash, A. Jr., 2005. Laboratory deformation of granular quartz sand: implications for the burial of clastic rocks, *AAPG Bull.,* **89**(5), 603–625.

Kemeny, J.M. & Cook, N.G., 1991. Micromechanics of deformation in rocks, in *Toughening Mechanisms in Quasi-Brittle Materials,* NATO ASI Series, pp. 155–188, ed. Shah, S.P., Springer.

Kümpel, H.-J., 1991. Poroelasticity: parameters reviewed, *Geophys. J. Int.,* **105**(3), 783–799.

Lehner, F. & Kachanov, M., 1996. On modelling of "winged" cracks forming under compression, *Int. J. Fract.,* **77**(4), R69–R75.

Liteanu, E., Spiers, C. & de Bresser, J., 2013. The influence of water and supercritical CO_2 on the failure behavior of chalk, *Tectonophysics,* **599,** 157–169.

Mallet, C., Fortin, J., Guéguen, Y. & Bouyer, F., 2013. Effective elastic properties of cracked solids: an experimental investigation, *Int. J. Fract.,* **182**(2), 275–282.

Mallet, C., Fortin, J., Guéguen, Y. & Bouyer, F., 2014. Evolution of the crack network in glass samples submitted to brittle creep conditions, *Int. J. Fract.,* **190**(1–2), 111–124.

Mavko, G., Mukerji, T. & Godfrey, N., 1995. Predicting stress-induced velocity anisotropy in rocks, *Geophysics,* **60**(4), 1081–1087.

Mavko, G., Mukerji, T. & Dvorkin, J., 1998. *The Rock Physics Handbook: Tools for Seismic Analysis in Porous Media,* 329 pp., Cambridge Univ. Press.

Miller, S.A., 2002. Properties of large ruptures and the dynamical influence of fluids on earthquakes and faulting, *J. geophys. Res.,* **107**(B9), ESE 3–1–ESE 3–13.

Murray, A.N., 1930. Limestone oil reservoirs of the northeastern United States and of Ontario, Canada, *Econ. Geol.,* **25**(5), 452–469.

Nagel, N., 2001. Compaction and subsidence issues within the petroleum industry: from Wilmington to Ekofisk and beyond, *Phys. Chem. Earth A,* **26,** 3–14.

Nasseri, M., Schubnel, A. & Young, R., 2007. Coupled evolutions of fracture toughness and elastic wave velocities at high crack density in thermally treated westerly granite, *Int. J. Rock Mech. Min. Sci.,* **44**(4), 601–616.

Olson, J.E., 2003. Sublinear scaling of fracture aperture versus length: an exception or the rule?, *J. geophys. Res.,* **108**(B9), doi:10.1029/2001JB000419.

Ougier-Simonin, A., Fortin, J., Guéguen, Y., Schubnel, A. & Bouyer, F., 2011. Cracks in glass under triaxial conditions, *Int. J. Eng. Sci.,* **49**(1), 105–121.

Paterson, M., 1958. Experimental deformation and faulting in Wombeyan marble, *Bull. geol. Soc. Am.,* **69**(4), 465–476.

Paterson, M., 1978. *Experimental Rock deformation: The Brittle Field,* Springer-Verlag.

Paterson, M.S. & Wong, T.-F., 2005. *Experimental Rock Deformation —The Brittle Field,* Springer-Verlag.

Peng, S. & Johnson, A., 1972. Crack growth and faulting in cylindrical specimens of chelmsford granite, *Int. J. Rock Mech. Min. Sci. Geomech. Abstr.,* **9**(1), 37–86.

Peška, P. & Zoback, M.D., 1995. Compressive and tensile failure of inclined well bores and determination of in situ stress and rock strength, *J. geophys. Res.,* **100**(B7), 12 791–12 811.

Pollard, D. & Segall, P., 1987. Theoretical displacements and stresses near fractures in rock: with applications to faults, joints, veins, dikes, and solution surfaces, *Fract. Mech. Rock,* **277**(349), 277–349.

Regnet, J., David, C., Fortin, J., Robion, P., Makhloufi, Y. & Collin, P., 2015a. Influence of microporosity distribution on the mechanical behavior of oolithic carbonate rocks, *Geomech. Energy Environ.,* **3,** 11–23.

Regnet, J., Robion, P., David, C., Fortin, J., Brigaud, B. & Yven, B., 2015b. Acoustic and reservoir properties of microporous carbonate rocks: implication of micrite particle size and morphology, *J. geophys. Res.,* **120**(2), 790–811.

Renshaw, C. & Park, J., 1997. Effect of mechanical interactions on the scaling of fracture length and aperture, *Nature,* **386,** 482–484.

Risnes, R., Madland, M., Hole, M. & Kwabiah, N., 2005. Water weakening of chalk—mechanical effects of water–glycol mixtures, *J. Pet. Sci. Eng.,* **48**(1), 21–36.

Robertson, E.C., 1955. Experimental study of the strength of rocks, *Bull. geol. Soc. Am.,* **66**(10), 1275–1314.

Røyne, A., Bisschop, J. & Dysthe, D.K., 2011. Experimental investigation of surface energy and subcritical crack growth in calcite, *J. geophys. Res.,* **116**(B4), doi:10.1029/2010JB008033.

Røyne, A., Dalby, K.N. & Hassenkam, T., 2015. Repulsive hydration forces between calcite surfaces and their effect on the brittle strength of calcite bearing rocks, *Geophys. Res. Lett.,* **42,** 4786–4794.

Rutter, E.H., 1972. The influence of interstitial water on the rheological behaviour of calcite rocks, *Tectonophysics,* **14**(1), 13–33.

Rutter, E.H., 1974. The influence of temperature, strain rate and interstitial water in experimental deformation of calcite rocks, *Tectonophysics,* **22,** 311–334.

Rutter, E.H., 1986. On the nomenclature of mode of failure transitions in rocks, *Tectonophysics,* **122**(3), 381–387.

Sayers, C.M. & Kachanov, M., 1995. Microcrack-induced elastic wave anisotropy of brittle rocks, *J. geophys. Res.,* **100**(B3), 4149–4156.

Scholle, P.A., Bebout, D.G. & Moore, C.H. (eds), 1983. *Carbonate Depositional Environments: AAPG Memoir 33,* no. 33, AAPG.

Schubnel, A., Walker, E., Thompson, B.D., Fortin, J., Guéguen, Y. & Young, R.P., 2006. Transient creep, aseismic damage and slow failure in Carrara marble deformed across the brittle-ductile transition, *Geophys. Res. Lett.,* **33**(17), L17301, doi:10.1029/2006GL026619.

Segall, P., 1989. Earthquakes triggered by fluid extraction, *Geology,* **17**(10), 942–946.

Shafiro, B. & Kachanov, M., 1997. Materials with fluid-filled pores of various shapes: effective elastic properties and fluid pressure polarization, *Int. J. Solids Struct.,* **34**(27), 3517–3540.

Shariatpanahi, S.F., Strand, S. & Austad, T., 2010. Evaluation of water-based enhanced oil recovery (EOR) by wettability alteration in a low-permeable fractured limestone oil reservoir, *Energy Fuels,* **24**(11), 5997–6008.

Sibson, R., 1982. Fault zone models, heat-flow, and the depth distribution of earthquakes in the continental-crust of the United-States, *Bull. seism. Soc. Am.,* **72,** 151–163.

Simmons, G. & Wang, H., 1971. *Single Crystal Elastic Constants and Calculated Aggregate Properties,* MIT Press.

Simpson, D., Leith, W. & Scholz, C., 1988. Two types of reservoir-induced seismicity, *Bull. seism. Soc. Am.,* **78**(6), 2025–2040.

Talwani, P. & Acree, S., 1984. Pore pressure diffusion and the mechanism of reservoir-induced seismicity, *Pure appl. Geophys.,* **122**(6), 947–965.

Turner, F.J., Griggs, D.T. & Heard, H., 1954. Experimental deformation of calcite crystals, *Bull. geol. Soc. Am.,* **65**(9), 883–934.

Vajdova, V., Baud, P. & Wong, T.-F., 2004. Compaction, dilatancy, and failure in porous carbonate rocks, *J. geophys. Res.,* **109**(B5), doi:10.1029/2003JB002508.

Vajdova, V., Zhu, W., Chen, T.-M.N. & Wong, T.-F., 2010. Micromechanics of brittle faulting and cataclastic flow in Tavel limestone, *J. Struct. Geol.,* **32**(8), 1158–1169.

Vajdova, V., Baud, P., Wu, L. & fong Wong, T., 2012. Micromechanics of inelastic compaction in two allochemical limestones, *J. Struct. Geol.,* **43**(0), 100–117.

Vincké, O., Boutéca, M. & Piau, J., 1998. Study of the effective stress at failure, in *Poromechanics, a Tribute to Maurice A. Biot,* pp. 635–639, eds Thimus J.-F. *et al.*, A.A. Balkema.

Violay, M., Nielsen, S., Spagnuolo, E., Cinti, D., Di Toro, G. & Di Stefano, G., 2013. Pore fluid in experimental calcite-bearing faults: abrupt weakening and geochemical signature of co-seismic processes, *Earth planet. Sci. Lett.,* **361,** 74–84.

Walsh, J.B., 1965. The effect of cracks on the compressibility of rock, *J. geophys. Res.,* **70**(2), 381–389.

Wang, X.-Q., Schubnel, A., Fortin, J., Guéguen, Y. & Ge, H.-K., 2013. Physical properties and brittle strength of thermally cracked granite under confinement, *J. geophys. Res.,* **118**(12), 6099–6112.

Winkler, K.W. & Murphy, W.F., 1995. Acoustic velocity and attenuation in porous rocks, in *Rock Physics & Phase Relations: A Handbook of Physical Constants,* pp. 20–34, ed. Ahrens, T.J., American Geophysical Union.

Wong, T.-F. & Baud, P., 2012. The brittle-ductile transition in porous rock: A review, *J. Struct. Geol.,* **44**(0), 25–53.

Wong, T.-F., Szeto, H. & Zhang, J., 1992. Effect of loading path and porosity on the failure mode of porous rocks, *Appl. Mech. Rev.,* **45,** 281–293.

Wong, T.-F., David, C. & Zhu, W., 1997. The transition from brittle faulting to cataclastic flow in porous sandstones: mechanical deformation, *J. geophys. Res.,* **102**(B2), 3009–3025.

Zhu, W., Baud, P. & Wong, T.-F., 2010. Micromechanics of cataclastic pore collapse in limestone, *J. geophys. Res.,* **115**(B4), doi:10.1029/2009JB006610.

Zimmerman, R.W., 1990. *Compressibility of Sandstones,* Elsevier.

APPENDIX A: CRACK DENSITY INVERSION

Axial crack densities were inverted from ultrasonic wave velocity measurements. Here, we recall the inversion process for dry solids but water-saturated solids can be considered in a similar manner (Shafiro & Kachanov 1997). First, the effective mechanical properties of the calcite aggregate composed of the solid matrix and embedded spherical pores were obtained by inverting the velocity data obtained at $P_c = 85$ MPa hydrostatic stress (beyond the crack closure pressure). The effective Young modulus E_0 and effective Poisson's ratio ν_0 are calculated as

$$\nu_0 = \left(\frac{1}{2}\left(\frac{V_p}{V_s}\right)^2 - 1\right) \Big/ \left(\left(\frac{V_p}{V_s}\right)^2 - 1\right), \tag{A1}$$

$$E_0 = 2\rho(1+\nu_0)V_s^2, \tag{A2}$$

where V_p, V_s and ρ are the P-wave velocity, S-wave velocity and the rock density, respectively. Rock density was obtained by weighting a dry sample. Using $V_p = 4350\,\mathrm{m\,s^{-1}}$, $V_s = 2350\,\mathrm{m\,s^{-1}}$, values obtained at $P_c = 85$ MPa, and $\rho = 2295\,\mathrm{kg\,m^{-3}}$, we get $E_0 = 32.8$ GPa, and $\nu_0 = 0.29$.

For a transverse isotropic symmetry along axis 3, the crack density tensor α is

$$\alpha = \begin{pmatrix} \alpha_{11} & 0 & 0 \\ 0 & \alpha_{11} & 0 \\ 0 & 0 & \alpha_{33} \end{pmatrix}, \tag{A3}$$

where α_{11} is the axial crack density and α_{33} is the radial crack density. In the case of the non-interacting approximation, the relation between the stiffness tensor C and α is given by (Sayers & Kachanov 1995):

$$\begin{cases} C_{11} + C_{12} = (1/E_0 + \alpha_{33})/D \\ C_{11} - C_{12} = 1/((1+\nu_0)/E_0 + \alpha_{11}) \\ C_{33} = ((1+\nu_0)/E_0 + \alpha_{11})/D \\ C_{44} = 1/(2(1+\nu_0)/E_0 + \alpha_{11} + \alpha_{33}) \\ C_{13} = (\nu_0/E_0)/D \\ C_{66} = 1/(2(1+\nu_0)/E_0 + 2\alpha_{11}) \end{cases} \tag{A4}$$

where

$$D = (1/E_0 + \alpha_{33})((1-\nu_0)/E_0 + \alpha_{11}) - 2(\nu_0/E_0)^2. \tag{A5}$$

From the effective stiffness tensor, we calculate the wave phase velocity along the propagation angles ϕ corresponding to our sensors setup (Mavko *et al.* 1998):

$$V_p(\phi) = [(C_{11}\sin^2(\phi) + C_{33}\cos^2(\phi) + C_{44} + \sqrt{M})/(2\rho)]^{1/2}, \tag{A6}$$

$$V_{sh}(\phi) = [(C_{11}\sin^2(\phi) + C_{33}\cos^2(\phi) + C_{44} - \sqrt{M})/(2\rho)]^{1/2}, \tag{A7}$$

$$V_{sv}(\phi) = [(C_{66}\sin^2(\phi) + C_{44}\cos^2(\phi))/\rho]^{1/2}, \tag{A8}$$

where

$$M = ((C_{11} - C_{44})\sin^2(\phi) - (C_{33} - C_{44})\cos^2(\phi))^2 + ((C_{13} + C_{44})\sin(2\phi))^2. \tag{A9}$$

We then use a least square procedure to compare predicted synthetic data and measured velocities. The inverted axial crack density corresponds to the value leading to the minimum distance between predicted and measured velocities.

APPENDIX B: PEAK STRESS MODEL

In the brittle regime, the evolution of the peak stress at failure with respect to the confining pressure is modelled by eq. (11). This equation is obtained using Ashby & Sammis' (1990) 2-D (plane strain) model. Wings are assumed to grow from initial cracks, which induces a crack density $D = \pi(l + a\cos\psi)^2 N_A$, where l is the length of the wing and N_A is the number of sliding cracks of uniform orientation ψ per unit area initially present. Before wings nucleate their length is $l = 0$ and the initial damage is $D_0 = \pi(a\cos\psi)^2 N_A$. The remotely applied principal stresses evolve with damage in accordance with eq. (17) of Ashby & Sammis (1990), written here with the convention of positive compression stresses:

$$\sigma_1 = \left(C_1 + \frac{C4(\sqrt{D/D_0} - 1)}{1 + \sqrt{\pi D_0}\frac{\sqrt{D/D_0}-1}{1-\sqrt{D}}} \right)\sigma_3 + \left(\frac{\sqrt{\sqrt{D/D_0} - 1 + 0.1/\cos\psi}}{1 + \sqrt{\pi D_0}\frac{\sqrt{D/D_0}-1}{1-\sqrt{D}}} \right)\left(\frac{C_4}{\sqrt{\cos\psi}} \right)\frac{K_{IC}}{\sqrt{\pi a}}, \tag{B1}$$

where

$$C_1 = \frac{\sqrt{1+\mu^2} + \mu}{\sqrt{1+\mu^2} - \mu}, \tag{B2}$$

and

$$C_4 = \frac{\sqrt{30}\cos\psi}{\sqrt{1+\mu^2} - \mu}. \tag{B3}$$

Specifying the material parameters D_0, $K_{IC}/(\pi a)^{1/2}$, and μ, the evolution of the principal stress σ_1 at a fixed confining pressure σ_3 can be calculated as a function of damage D using eq. (B1). At some point, the stress attains a peak beyond which instability sets in. The calculation can be repeated for different values of fixed confining pressure σ_3, which allows to map out the peak stress at failure in the P–Q map (Fig. 13).

APPENDIX C: ADDITIONAL MECHANICAL DATA

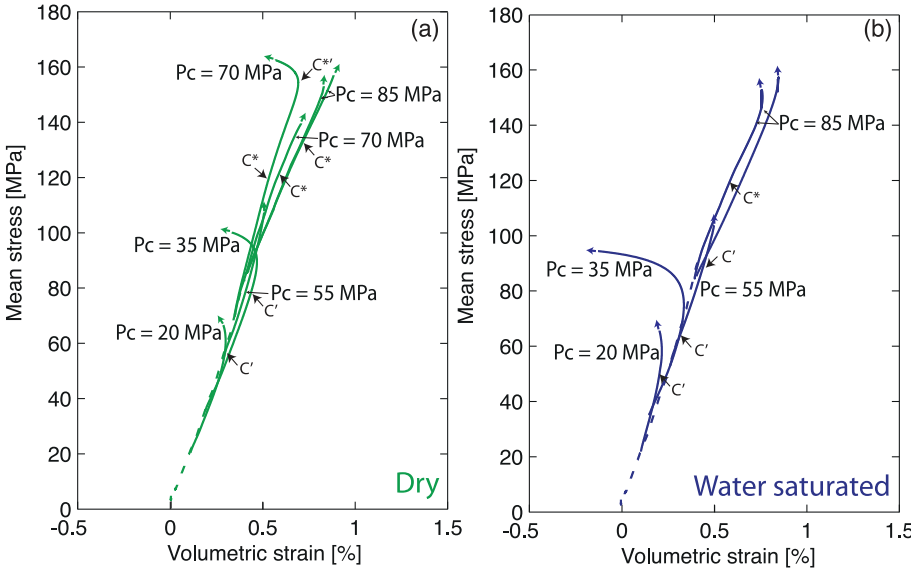

Figure C1. Compilation of mechanical data for experiments reported in Table 2. The mean stress is plotted versus volumetric strain for (a) dry and (b) water-saturated experiments performed at 20 °C. Stress states at the onset of dilatancy C', onset of inelastic compaction C^* and post-yield onset of dilatancy $C^{*\prime}$ are shown for references on some experiments. Arrows mean that samples did not attain failure and could experience further deformation.